Speleothem evidence for late Miocene extreme Arctic amplification - an analogue for near future anthropogenic climate change?

Stuart Umbo[1], Franziska Lechleitner[2], Thomas Opel[3], Sevasti Modestou[1], Tobias Braun[4,5], Anton Vaks[6], Gideon Henderson[7], Pete Scott[8], Alexander Osintzev[9], Alexandr Kononov[10,11], Irina Adrian[12], Yuri Dublyansky[13], Alena Giesche[14, 15], Sebastian F.M. Breitenbach[1]

[1]Department of Geography and Environmental Sciences, Northumbria University, Newcastle-upon-Tyne, NE1 8ST, United Kingdom
[2]Department of Chemistry, Biochemistry and Pharmaceutical Sciences & Oeschger Centre for Climate Change Research, Bern, 2012, Switzerland
[3]Alfred Wegener Institute Helmholtz Centre for Polar and Marine Research, Telegrafenberg A45, Potsdam, 14473, Germany
[4]Remote Sensing Centre for Earth System Research, Leipzig University, 04103, Leipzig, Germany
[5]Potsdam Institute for Climate Impact Research (PIK), Member of the Leibniz Association, 14473, Potsdam, Germany
[6]Geochemistry and Environmental Geology Division, Geological Survey of Israel, Jerusalem, 9692100, Israel
[7]Department of Earth Sciences, Oxford University, Oxford, OX1 3AN United Kingdom
[8]Oceans Institute, University of Western Australia, Perth, 6009, Australia
[9]Speleoclub Arabika, Irkutsk, 664058, Russian Federation
[10]Irkutsk Nation al Research Technical University, Irkutsk, 664074, Russia
[11]Institute of the Earth's Crust, Russian Academy of Sciences, Siberian Branch, Irkutsk, 664033, Russia
[12]Lena Delta Wildlife Reserve, Tiksi, Sakha Republic, 678400 Russia
[13]Institute of Geology, University of Innsbruck, Innrain 52, 6020, Innsbruck, Austria
[14]U.S. Geological Survey, Alaska Science Center, Anchorage, Alaska 99508, USA
[15]Department of Earth Sciences, Cambridge University, Cambridge CB2 3EQ, United Kingdom

Correspondence to: Stuart Umbo (stuart.umbo@northumbria.ac.uk)

Abstract. The Miocene provides an excellent climatic analogue for near future anthropogenic warming, with atmospheric CO_2 concentrations and global average temperatures similar to those projected for the coming century. However, the magnitude of Miocene Arctic warming remains unclear due to the scarcity of reliable proxy data. Here we use stable oxygen isotope and trace element analyses, alongside clumped isotope and fluid inclusion palaeothermometry of speleothems to reconstruct palaeo-environmental conditions near the Siberian Arctic coast during the late Tortonian (8.68 ± 0.09 Ma). Stable oxygen isotope records suggest warmer than present temperatures. This is supported by temperature estimates based on clumped isotopes and fluid inclusions giving mean annual air temperatures between +6.6 and +11.1°C, compared with -12.3°C today. Trace elements records reveal a highly seasonal hydrological environment.

Our estimate of >18°C of Arctic warming supports the wider consensus of a warmer-than-present Miocene and provides a rare paleo-analogue for future Arctic amplification under high emissions scenarios. The reconstructed increase in mean surface temperature far exceeds those projected in fully coupled global climate models, even under extreme emissions scenarios. Given that climate models have consistently underestimated the extent of recent Arctic amplification, our proxy data suggest Arctic warming may exceed current projections. If Arctic warming by 2100 matches our late Miocene estimates, it would have large-scale impacts on global climate, including extensive thawing of Siberian permafrost – a vast fossil carbon store.

1 Introduction

The Arctic and sub-Arctic regions have warmed nearly four times faster than the global average since 1979 (Rantanen et al., 2022), and this disproportionate warming is expected to continue over the coming decades (Ma et al., 2022). Climate models have consistently underestimated the magnitude of this so-called Arctic amplification (Chylek et al., 2022; Rantanen et al., 2022) and show considerable discrepancies in its predicted magnitude (Smith et al., 2020; Taylor et al., 2022). Uncertainty in Arctic temperature projections are greater than for any other region on the planet (Taylor et al., 2022).

The Arctic is home to most of the global permafrost, a crucial climate tipping element (McKay et al., 2022). The Earth's largest terrestrial carbon pool (Strauss et al., 2024), thawing permafrost will play a major role in future climate trajectories. Permafrost degradation is occurring much faster, and earlier, than expected (Farquharson et al., 2019). Increasing air temperatures lead to higher permafrost temperatures: a global network of borehole measurements over the period 2007 to 2016 show warming of 0.39 ± 0.15°C in pan-Arctic continuous permafrost (Biskaborn et al., 2019). Satellite data show large increases in thermokarst thaw slump rate and prevalence in Canada (Lewkowicz & Way, 2019) and east Siberia, alongside extensive methane emissions from thawing hydrate deposits in northern Siberia (Froitzheim et al., 2021). Yet, the regional impacts and carbon cycle feedbacks of thawing permafrost are highly uncertain and remain a key unknown in climate models (Damon Matthews et al., 2021).

Temperature has long been considered the main driver of permafrost stability, but recent studies have demonstrated the importance of seasonal precipitation characteristics, with increased rainfall amount and reduced snowfall duration driving permafrost degradation (Kokelj et al., 2015; O'Neill & Burn, 2017). The poorly constrained regional precipitation response to Arctic amplification (Bintanja et al., 2020), alongside limited understanding of localised feedbacks and natural variability (Taylor et al., 2022) hinder estimations of future permafrost thaw. Best estimates project the extent of global thaw between 2 and 66 % by 2100, even with concerted action to decarbonise society (IPCC, 2019). This wide range arises in part from the fact that current global climate models largely neglect feedbacks from permafrost thaw (Nazarenko et al., 2022). Thus, permafrost-sourced greenhouse gas (GHG) emissions are not considered in targets set under the 2015 Paris Agreement (Gasser et al., 2018). Permafrost-derived GHGs could account for up to 8% of total permissible emissions (the emissions budget) if global warming is to remain below the United Nations (UN) 2°C target (Gasser et al., 2018). Subsequent studies have suggested that permafrost emissions could be even higher due to abrupt permafrost thaw (Turetsky et al., 2020). Better understanding of both Arctic temperature amplification and hydrological changes in response to warming is therefore of great importance for improving projections of permafrost thaw. Detailed paleoclimate records from Arctic speleothems (carbonate cave deposits) present an excellent opportunity to verify climate models and improve future projections. This is because they can concurrently resolve the variables of temperature, precipitation, and the presence or absence of (continuous) permafrost. Since speleothem deposition requires liquid dripwater and permafrost is largely impermeable, periods of speleothem formation indicate the absence of continuous permafrost in regions of modern-day permafrost stability (Vaks et al., 2013, 2020).

Arctic warming has consistently exceeded the Northern Hemisphere mean by a factor of 3 - 4 during Quaternary interglacials (Miller et al., 2010). Recently, Steinthorsdottir and colleagues (2021) proposed the Miocene (23.03 - 5.33 Ma) as a suitable palaeo-analogue for anthropogenic climate change. Late Miocene (ca. 7 - 5.4 Ma) atmospheric carbon dioxide concentrations are estimated between 400 - 600 ppm (Rae et al., 2021), i.e., similar to modern levels and those projected for the coming decades at current emission rates (Masson-Delmotte et al., 2021). The distribution of continental landmasses was similar to the modern day (Steinthorsdottir et al., 2021), and temperatures were considerably warmer. Global mean sea surface temperature (SST) was ca. 6°C higher than present day (Herbert et al., 2016), and mean terrestrial surface temperature was ca. 4.5°C above the pre-industrial level (Pound et al., 2011).

Here we present a multi-proxy analysis of four speleothems from the Siberian Arctic to infer environmental conditions during the Tortonian (late Miocene). We use isotope measurements of speleothem fluid inclusions and clumped isotope analyses to estimate palaeotemperatures during periods of permafrost absence, and stable oxygen isotope and trace element data to reconstruct palaeo-hydrology and seasonality. We utilise these high latitude temperature reconstructions to provide an estimate of future permafrost thaw assuming similar levels of Arctic warming in the near future.

2 Study site and sample material

2.1 Study site

Samples were collected from the Taba Bastaakh cliffs (N72.27°, E126.94°), which rise ca. 140 m above the eastern riverbank near the entrance of the Lena River delta, ca. 100 km northwest of Tiksi, Sakha Republic, Russian Federation (Fig. 1). The

100 cliffs are composed of Carboniferous-aged carbonates (Mikhaltsov et al., 2018). Lower strata (up to ca. 50 m above current river level) comprises fine quartzitic sandstone, siltstone, sandy dolomite, and dolomitic limestone with sparse fossil coral and ostracod and foraminifera assemblages broadly linked to the Tournaisian (358.9–346.7 Ma) (Izokh & Yazikov, 2017). Above, ca. 50 m from the riverbank, bioclastic carbonate, calcareous siliciclastics and carbonates form a subsiding platform. Continuous permafrost, 400–600 m thick, is found in this region, with an active layer thaw depth between 0.6 and 0.4 m (Boike

105 et al., 2019). All caves encountered during the expedition contained significant ice deposits, rendering modern speleothem formation impossible. Modern tundra vegetation is sparse, consisting mostly of flowers, grasses, mosses, and lichens. Trees are not found above the caves today.
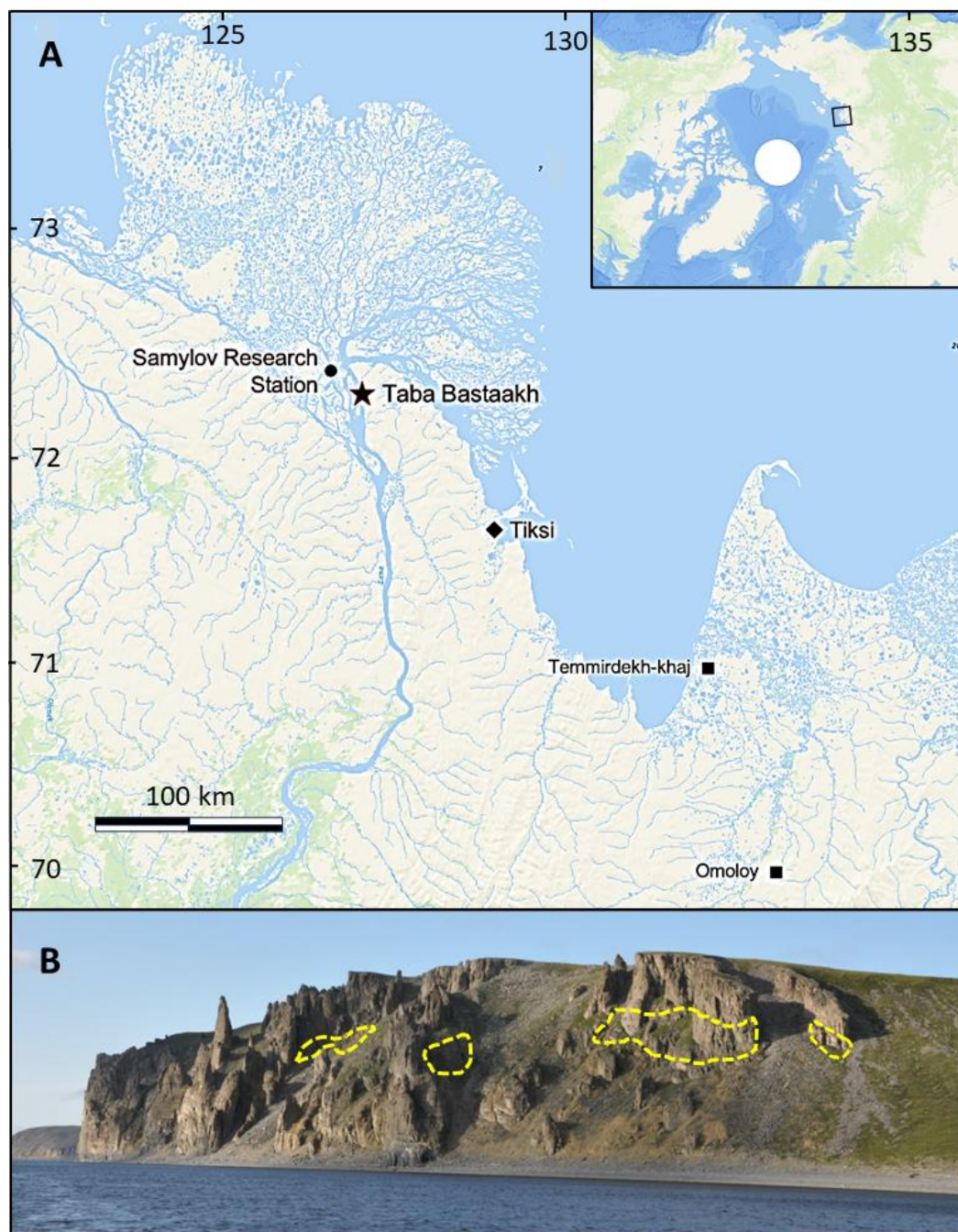
Figure 1: (A) Location of Taba Bastaakh sampling site, Samoylov Research Station, and relevant Miocene palaeoclimate reconstruction sites: Temmirdekh-khaj and Omoloy (Popova et al., 2012) (Map created in Esri ArcGIS), (B) Photograph of the Taba Bastaakh cliffs with cave locations outlined with yellow dashed lines (adapted from Vaks et al., in review).

Meteorological data recorded at the Samoylov Island Research Station in the central Lena River Delta (N72.37°, E126.48°), ca. 20 km northwest of our study area, indicate a polar tundra climate (ET according to the Köppen-Geiger classification, Peel

115   et al., (2007)), with a mean annual air temperature (MAAT) of -12.3°C, July average of +9.5°C, and February average of – 32.7°C (all temperature data averaged between 1998 and 2017) (Boike et al., 2019). Mean annual rainfall (2002 - 2017) is 169 mm and mean annual snow cover 0.3 m (Boike et al., 2019).

2.2 Sample description

Fourteen speleothem samples were collected from the base of the Taba Bastaakh cliffs, on the bank of the Lena River in 2014.

120   Today, the caves are ice filled and inaccessible, but erosion of the cliff face has exposed relic caves with speleothems observed along the cliff walls. Observations of ongoing weathering of cave walls suggest that these samples originated from the cliff face 70-120 m above the sampling site. All 14 samples have been previously dated to the Tortonian stage using U-Pb dating following a modified method described in (Vaks et al., 2020) and (Mason et al., 2022). The ^{235}U-^{207}Pb – ^{208}Pb/^{207}Pb isochron age of all samples yielded an age of 8.68 ± 0.09 Ma with a mean square weighted deviation of 1.2 (Vaks et al., in review).

125   Overlapping uncertainties of top and bottom ages allow only the construction of relative age-depth models along the growth profile of individual samples.

Four samples, STBB I – 1, STBB II – 7, STBB 4 – 2, and STBB 4 – 3 (Fig. 2) were selected for further study, as their high precision dates and large size make them amenable for coupled reconstruction of temperature and climate conditions at their

130   time of deposition. All samples are composed of calcite (Vaks et al., in review).
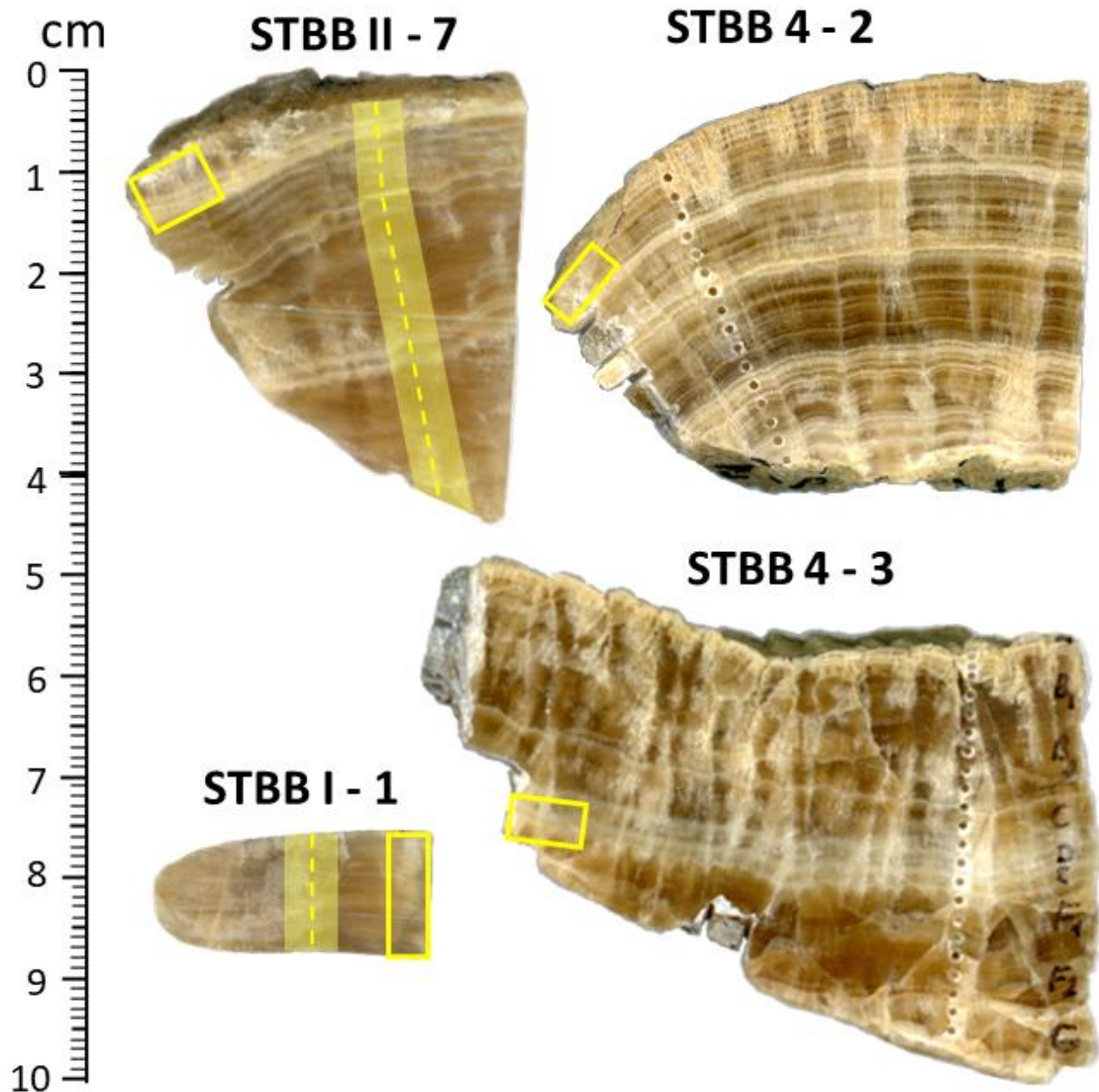
Figure 2: Speleothem samples used in this study. Thick translucent tracks, overlain with dashed lines, show the positions of stable isotope and trace element sampling profiles respectively (STBB I – 1 and STBB II – 7 only). Boxes indicate clumped isotope sampling positions.

3 Methodology

3.1 Clumped isotope geothermometry

Clumped isotope analyses for estimating speleothem formation temperatures were performed on subsamples of all four speleothems. Measurements were conducted at Northumbria University using a Nu Instruments Perspective dual inlet isotope ratio mass spectrometer coupled with an automated NuCarb preparation system. Samples were drilled from layers with well constrained ages and 325 ± 25 µg of powder loaded into sample vials, which were then evacuated, and reacted with concentrated orthophosphoric acid at 70°C. The reactant gas was dehydrated and cleaned using standard procedures (Petersen et al., 2015). Briefly, samples were dehydrated using two liquid nitrogen cryotraps, cooled to -80°C, and scrubbed of contaminants by passing through a 1 cm static trap filled with a Porapak™ Q (Waters Corporation) absorbent material, cooled to -30°C. Each replicate digestion was measured 40 times in dual inlet mode (total measurement time ca. 40 minutes). No pressure baseline correction was required.

Final Δ_{47} values were calculated using the software Easotope (www.easotope.org; John & Bowen, 2016) using the IUPAC parameters for ^{17}O correction and isotopic ratios for VPDB and VSMOW (Bernasconi et al., 2018; Brand et al., 2010; Daëron et al., 2016). Sample Δ_{47} values were projected onto carbon dioxide equilibrium space (ICDES-90) following the methodology of Dennis et al. (2011), using standards ETH1, ETH2, and ETH3, and ICDES Intercarb Δ_{47} values from Bernasconi et al. (2021). Long term instrument performance was monitored with an internal standard, Pol-2 (a natural cave pool rim deposit), giving a long-term Δ_{47} external standard deviation of 0.032 ‰ (Δ_{47} = 0.656 ± 0.003 ‰ ICDES-90, $T_{\Delta_{47}}$ = 2.4 ± 1.0 °C, N = 65).

Replicates were measured across multiple runs over a long period of time, similar to the sliding window approach employed by, e.g., Meinicke et al. (2020) and described by Daëron & Gray (2023). Stable isotope and Δ_{47} outliers ($> \overline{x} \pm 2\sigma$), alongside samples with elevated Δ_{48}, indicative of contamination (Eiler & Schauble, 2004), were discarded from final Δ_{47} calculations (Table S4). After pruning, a minimum of 14 replicate analyses were made for each sample such that Δ_{47} 95 % confidence intervals of ≤0.015 ‰ were achieved (i.e., ≤0.007 ‰ standard error). All Δ_{47} uncertainties are quoted as standard errors and 95% confidence intervals, according to best practices outlined by Fernandez et al. (2017).

Clumped isotope temperatures ($T_{\Delta_{47}}$) were calculated using the composite regression of Anderson et al. (2021) and an internal laboratory calibration derived from 17 natural inorganic calcite samples precipitated at known temperatures (Fig. S1, Tables S1 and S2). The derived regression equation, calculated using the York least squares method (York et al., 2004) in the R geostats package, is:

$$\Delta_{47} = 0.0372 \, (\pm 0.0008) \cdot \frac{10^6}{T^2} + 0.166 \, (\pm 0.01) \qquad (1)$$

Bracketed numbers denote one standard error. The in-house regression has a slightly lower gradient and higher intercept than the composite regression derived by Anderson et al. (2021) (gradient = 0.0391 ± 0.0004, intercept = 0.154 ± 0.004). Measurement and calibration uncertainties were propagated together to calculate temperature uncertainty according to the
170 methods of Huntington et al. (2009).

3.2 Fluid inclusion analysis for temperature estimation

Fluid inclusion analyses were conducted on STBB I - 1 and STBB II - 7, where microscopic inspection confirmed the presence of fluid inclusions. Measurements were performed at the University of Innsbruck, Austria following the method of Dublyansky and Spötl, (2009). An aliquot of 1.5 g of carbonate was crushed in a heated crusher under He flow. The released fluid inclusion
175 water was cryo-trapped and then admitted into the TC/EA analyser (Thermo Scientific). After pyrolysis on contact with glassy carbon at 1400°C, the evolved H_2 and CO were separated in the GC column and admitted to a Delta V Advantage mass spectrometer (Thermo Scientific). Calibration was performed by measuring various amounts of reference waters with isotopic compositions bracketing the expected compositions of the sample. Fluid inclusion isotope data are reported with respect to. VSMOW. Accuracy of the measurement is 1.5 ‰ for δ^2H and 0.2 ‰ for $\delta^{18}O$.
180

Temperatures from fluid inclusions were calculated using the calibrations of (Tremaine et al., 2011) and (Coplen, 2007) for water-calcite oxygen isotope fractionation.

3.3 Stable oxygen and carbon isotopes

Samples STBB I – 1 and STBB II – 7 were micromilled at 50 µm resolution along their growth length using a Sherline
185 micromill, following the methodology outlined in Lechleitner et al. (2020), producing a total of 225 and 823 subsamples, respectively.

Stable isotope analysis was conducted at Northumbria University using a method adapted from Spötl & Vennemann, (2003). 110±10 µg of sample was loaded into a 12 ml borosilicate exetainer tube, flushed with helium and reacted with concentrated
190 orthophosphoric acid at 70°C. Liberated CO_2 was dried using a Gasbench II and analysed for carbon and oxygen isotope ratios. All samples were measured on a ThermoScientific Delta V Isotope Ratio Mass Spectrometer coupled with a ConFlo IV. We use an in-house laboratory carbonate standard (Plessen), alongside international standards NBS18 and IAEA603, measured every 10 samples to evaluate the runs. An in-house carbonate standard (Pol-2) was used to evaluate long-term external standard deviation, achieving <0.1 ‰ for $\delta^{18}O$. All carbonate derived stable isotope data is reported on the VPDB scale.

3.4 Trace element analysis

Trace element to calcium (X/Ca) ratios of 24 trace elements (tables S7 and S8) were measured along the stable isotope sampling profiles of STBB I – 1 and STBB II -7 at 2.6 μm resolution, using laser ablation inductively coupled plasma mass spectrometry (LA-ICP-MS) at the University of Western Australia following the methods outlined in Finestone et al. (2022).

We prioritised elements regularly utilised as hydrological proxies including Mg, Sr, and Ba (Stoll et al., 2012; Treble et al., 2015), alongside a vegetation proxy (P), indicators for detrital input (Al, Th) and heavy metals (Fe, Mn) associated with organic matter binding (Hartland et al., 2012). See supplementary tables S7 and S8 for a full list of elements analysed. The stable isotope record was aligned to the trace element record using multiple visual markers such as prominent growth layers and surface blemishes.

3.5 Permafrost vulnerability modelling

We use our Miocene temperature reconstructions to update the Vaks et al. (in review) estimates of permafrost thaw vulnerability and the resultant potential carbon emissions if similar levels of warming were observed in the modern day. Using the 1991-2020 Global Historical Climatology Network (GHCN) land temperature dataset (Fan & van den Dool, 2008), we identified permafrost regions vulnerable to thaw under different warming scenarios. Following the approach of Vaks et al. (in review), we overlaid vulnerable permafrost regions with modelled soil carbon content in the top 3 m of permafrost (Palmtag et al., 2022) using QGIS to estimate potential soil organic carbon (SOC) emissions from the thawing region. Given the reconstructed warming from the Taba Bastaakh samples, we estimated the land area that would warm above a MAAT of 0°C. The total SOC of the top 3 m in this area was summed, and a final estimate of emissions calculated assuming that 5-15% of the SOC would be released to the atmosphere as carbon emissions, following Schuur et al. (2015).

4 Results

4.1 Clumped isotope temperature estimates

Clumped isotope results are summarised in Table 1. The Δ_{47} values range from 0.626 to 0.641, returning clumped isotope temperature ($T_{\Delta 47}$) estimates between 6.6 and 11.1°C, using our in-house calibration. Standard errors in Δ_{47} are between 0.006 and 0.007 ‰ (95% confidence limits between 0.012 and 0.014 ‰, translating to a temperature uncertainty of < 2.4°C).

225 **Table 1: Clumped isotope data and temperature estimates from Taba Bastaakh samples. N = number of replicate Δ47 measurements included in final Δ47 calculations, with the number of excluded samples in parentheses. See section 3.1 for uncertainty calculations. The fluid inclusion temperature (TFI) from STBB I - 1 is presented for comparison with temperature range in parentheses. Replicate measurement data is presented in Table S3.**

Sample	N (Δ_{47})	Δ_{47} (‰, CDES90)	Δ_{47} SE (‰)	Δ_{47} 95% CI (‰)	$T_{\Delta47}$ (°C)	$T_{\Delta47}$ uncertainty (°C)	T_{FI} (°C) Tremaine	T_{FI} (°C) Coplen
STBB I - 1	21 (5)	0.626	0.007	0.015	11.1	2.1	9.0 – 19.2 (mean = 11.8)	10.9 – 21.5 (mean = 14.5)
STBB II - 7	18 (2)	0.641	0.006	0.012	6.6	1.8	NA	N/A
STBB 4-2	14 (3)	0.640	0.007	0.014	7.0	2.0	NA	N/A
STBB 4 - 3	14 (2)	0.634	0.007	0.014	8.7	2.4	NA	N/A

230 **4.2 Fluid inclusion temperature estimate**

Sample STBB I – 1 yielded 0.11 µL of fossil water with a $\delta^{18}O$ value of -17.5 ‰ VSMOW and a δD value of -127.7 ‰ VSMOW, giving a deuterium excess value (d-excess) of 12.3 ‰. This value lies within uncertainty of the modern Global Meteoric Water Line (GMWL) (Craig, 1961), and ca. +9 ‰ in δ^2H above the modern Local Meteoric Water Line (LMWL) from the Samoylov Island Research Station (Spors, 2018) (Fig. S2). Since large sample volumes are required for fluid inclusion

235 measurements, our $\delta^{18}O$ value is obtained from a speleothem section incorporating the entire growth length, representing an average of the entire speleothem. Thus, we applied a constant $\delta^{18}O$ value of -17.5 ‰ (VSMOW) for dripwater ($\delta^{18}O_{dw}$) across the entire calcite $\delta^{18}O$ record to obtain minimum and maximum temperature estimates. Sample STBB II – 7 failed to yield sufficient inclusion water for analysis and thus no temperature estimate could be derived from this sample. The lower end of the STBB I-1 fluid inclusion derived temperature estimate (T_{FI} = 9.0 – 19.2°C) overlaps with the independently derived $T_{\Delta47}$

240 estimate ($T_{\Delta47}$ = 11.1).

4.3 Stable oxygen isotopes

Speleothem $\delta^{18}O$ ranges between -17.5 and -14.6 ‰ VPDB, with mean values of -15.6 ‰ and -16.9 ‰ for STBB II – 7 and STBB I – 1, respectively (Fig. 3). STBB I – 1 $\delta^{18}O$ exhibits an initial decline, reaching a minimum around 4mm where the trend reverses. A sharp increase is observed around 7 mm where the record peaks and remains relatively constant thereafter.

245 The STBB II - 7 $\delta^{18}O$ record exhibits a similar initial decline of ca. 1 ‰ until ca. 20 mm, where this trend reverses. At ca. 37 mm $\delta^{18}O$ declines by ca. 1 ‰ in the final ca. 4 mm of the record.
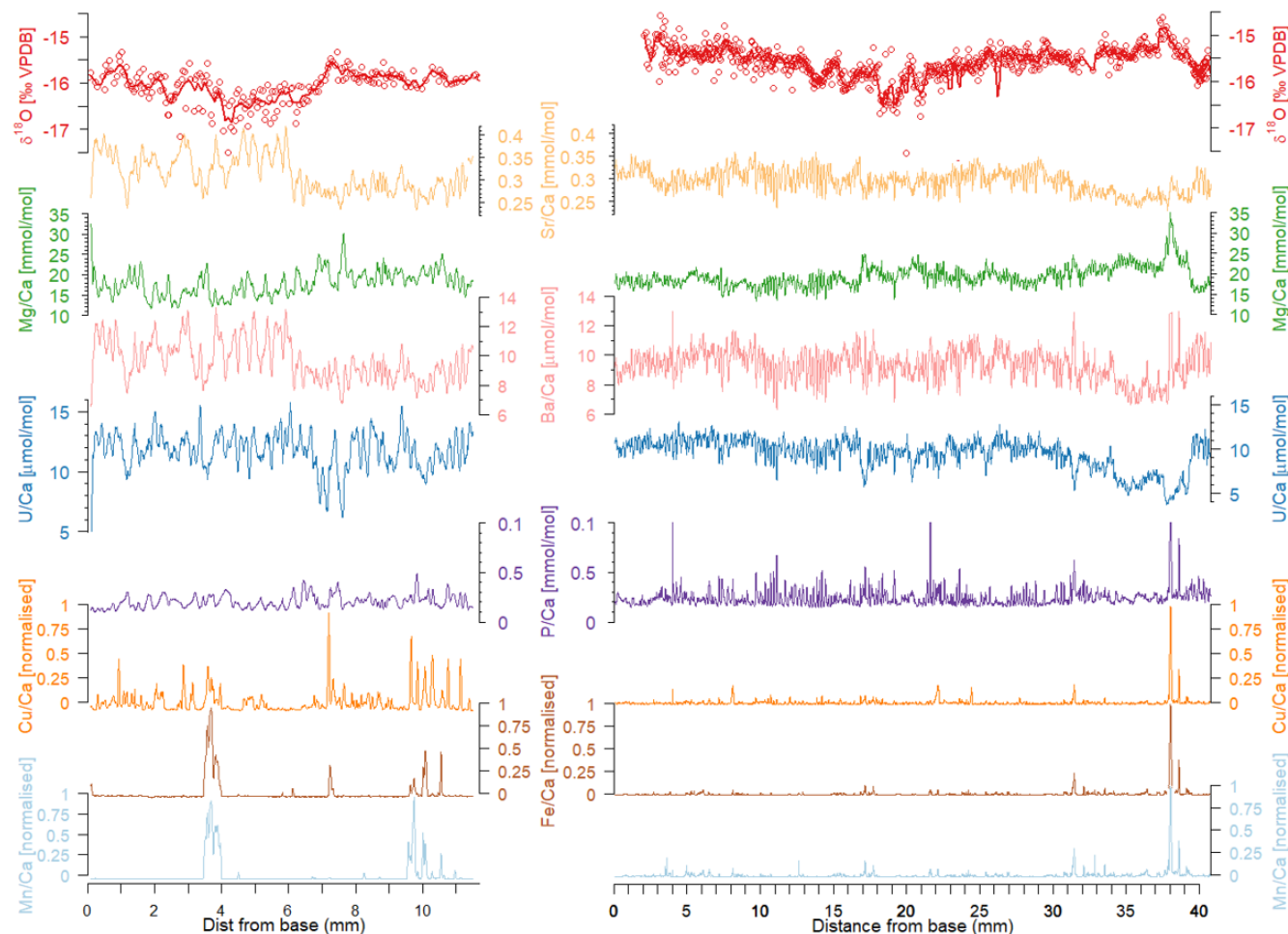
Figure 3: δ¹⁸O and selected trace element records for STBB I – 1 and STBB II – 7. δ¹⁸O data are shown with a 0.25 mm rolling window smoothing (thick lines). Trace elements are smoothed to 0.01 mm rolling window. Cu/Ca. Fe/Ca, and Mn/Ca ratios have been mean normalised for easier comparison between the two samples.

4.4 Trace elements

Our analysis focuses on 18 elements, predominantly cation substitutes Ba, Mg, Sr, U, and metals Cu, Co, Fe, and Mn. Concentrations of Y, La, Ce, Nd, Yb, and Th were below the detection limit and thus these elements were removed from subsequent analysis.

We utilised principal component analysis (PCA) to identify common variability in the Taba Bastaakh trace element records (Orland et al., 2014). A Gaussian kernel smoothing was applied to trace element records to remove missing data and minimise noise artefacts, before log transformation and z-score normalisation to account for the PCA's sensitivity to variable scaling. The PCA analysis was performed using the FactoMineR package in R.

We identify two dominant principal components (PCs) in each sample, accounting for 55.5 and 70.2 % of the variance in STBB I – 1 and STBB II – 7 respectively (Table 2, Fig. S3). These PCs highlight two elemental groupings, the first is defined by correlations with Ba, Sr, Mg, and U and accounts for 37 % of the variance in STBB I – 1 and 15.8 % in STBB II - 7. These

265 elements are commonly utilised as hydrological proxies in speleothems (Tooth & Fairchild, 2003; Treble et al., 2015) and we therefore refer to this PC as the hydrological PC. This PC also correlates with Na, P, and S in STBB I – 1. The second PC is defined by correlations with B, Fe, Mn, and Pb in both samples (Al, Cu, Co, Li, P, and Rb are also included in STBB II – 7) and accounts for 18.5 % of the variance in STBB I – 1 and 54.4 % in STBB II - 7. These elements are commonly associated with detrital input via flushing (Hartland et al., 2012) and we therefore refer to this PC as the detrital PC herein.

270

We applied spectral analysis to the smoothed trace element and isotope records to reveal periodicities and dominant frequencies along the speleothem growth length. This revealed strong cyclicity in the hydrological PC elemental ratios (Ba, Mg, Sr, and U) in both samples, with dominant frequencies at ~ 0.3 mm and 0.5 mm in STBB I – 1, and 0.2 mm in the STBB II – 7 (Fig. S5). We also observe cyclicity in P and Cu. Detrital PC metals remain relatively constant with sporadic spikes (Fig. 3).

275

Table 2: Results of multivariate principal component analysis on Taba Bastaakh speleothem samples. Two major elemental groupings are highlighted: The hydrological principal component, defined by elements Ba, Mg, P, Sr, U and the detrital principal component defined by elements Al, B, Cu, Co, Fe, Mn, Rb, Pb. An additional principal component (PC2) is identified in STBB I - 1 but is not explored further.

STBB I - 1			STBB II - 7		
	% of variance explained	Elements		% of variance explained	Elements
Hydrological principal component	37	Ba, Cu, Mg, Na, P, S, Sr, U	Hydrological principal component	15.8	Ba, Mg, Sr, U
Detrital principal component	18.5	B, Fe, Mn, Pb	Detrital principal component	54.4	Al, B, Cu, Co, Fe, Li, Mn, P, Rb

280 **5 Discussion**

The late Miocene is widely accepted to have been several degrees warmer than today. Global SSTs were ca. 6°C warmer than present (Herbert et al., 2016) and mean global surface temperature was ca. 4.5°C above pre-industrial (1870-1900) (Pound et al., 2011). Most temperature estimates for the Miocene stem from marine sediments, and terrestrial data from high northern latitudes are exceedingly sparse (e.g., Popova et al., 2012). Our speleothem records give a rare insight into terrestrial high

285 latitude environmental changes, including temperature and hydrological conditions during this period.

Taba Bastaakh lies deep within the modern continuous permafrost zone with a MAAT of -12.3°C. The regional modern annual ground temperature (MAGT) is -8.4°C, averaged along a 27 m borehole at the Samoylov Island Research Station (Boike et al., 2013). Since speleothem growth depends on liquid water supply, their presence at Taba Bastaakh indicates a much warmer

290 climate at the time of their formation (8.68 ± 0.09 Ma).

5.1 Quantitative Tortonian temperature estimates

We obtain quantitative estimates of Arctic temperatures at Taba Baastakh during the Tortonian between 6.6°C and 11.1°C, based on speleothem clumped isotopes and fluid inclusion isotopic analysis. The large sample sizes required for clumped isotope analysis (ca. 4 mg) make sampling of individual growth layers impossible and thus our temperature estimates derive

295 multi-annual means.

Table 3: Comparison of Taba Bastaakh temperature estimates derived from different calibrations. $T_{\Delta47}$ (this study) is compared with $T_{\Delta47}$ derived from the composite calibration of Anderson et al. (2021). Anderson derived $T_{\Delta47}$ uncertainties are calculated by propagating calibration uncertainties and Δ_{47} standard errors. T_{FI} is calculated using the calibrations of Tremaine et al. (2011) and
300 **Coplen (2007) with a constant $\delta^{18}O_{dw}$ of -17.5 ‰ (VSMOW) applied across the entire growth length.**

Sample name	$T_{\Delta47}$ (°C) This study	$T_{\Delta47}$ Uncertainty (°C) This study	$T_{\Delta47}$ (°C) Anderson	$T_{\Delta47}$ Uncertainty (°C) Anderson	T_{FI} (°C) Tremaine	T_{FI} (°C) Coplen
STBB I - 1	11.1	2.1	14.6	2.9	9.0 – 19.2 (mean = 11.8)	10.9 – 21.5 (mean = 14.5)
STBB II - 7	6.6	1.8	10.1	2.2	N/A	N/A
STBB 4 - 2	7.0	2.0	10.5	2.3	N/A	N/A
STBB 4 - 3	8.7	2.4	12.1	3.1	N/A	N/A

For comparison we calculated our clumped isotope temperatures with both our in-house calibration (section 3.1) and the composite calibration of Anderson et al. (2021). $T_{\Delta47}$ estimates derived using the Anderson et al. (2021) calibration are consistently higher than values derived from our own calibration by an average of 3.5°C (Table 3). We suggest that the steeper

305 gradient (+0.0391 ± 0.0004) and lower intercept (0.154 ± 0.004) of Anderson et al. (2021) are influenced by five of their calibration samples formed at high temperatures (>252°C). Thus, we utilise our in-house calibration, which is derived solely from subaqueous cave carbonates precipitated at temperatures similar to our samples, for final temperature reconstructions. This gives more conservative (i.e., lower) temperature estimates compared to those based on the Anderson et al. calibration.

310 Our dataset allows for a direct comparison between clumped isotope and fluid inclusion-based temperature estimates on one sample (STBB I-1), with the $T_{\Delta47}$ estimate (11.1 ± 2.1°C) overlapping with the T_{FI} estimates of both Tremaine et al. (2013)

(9.0 – 19.2°C, mean = 11.8°C) (Table 3) and Coplen et al. (2007) (10.9 - 21.5°C, mean = 14.5°C) calibrations. A full discussion of temperature reconstruction uncertainties is given in the SOM.
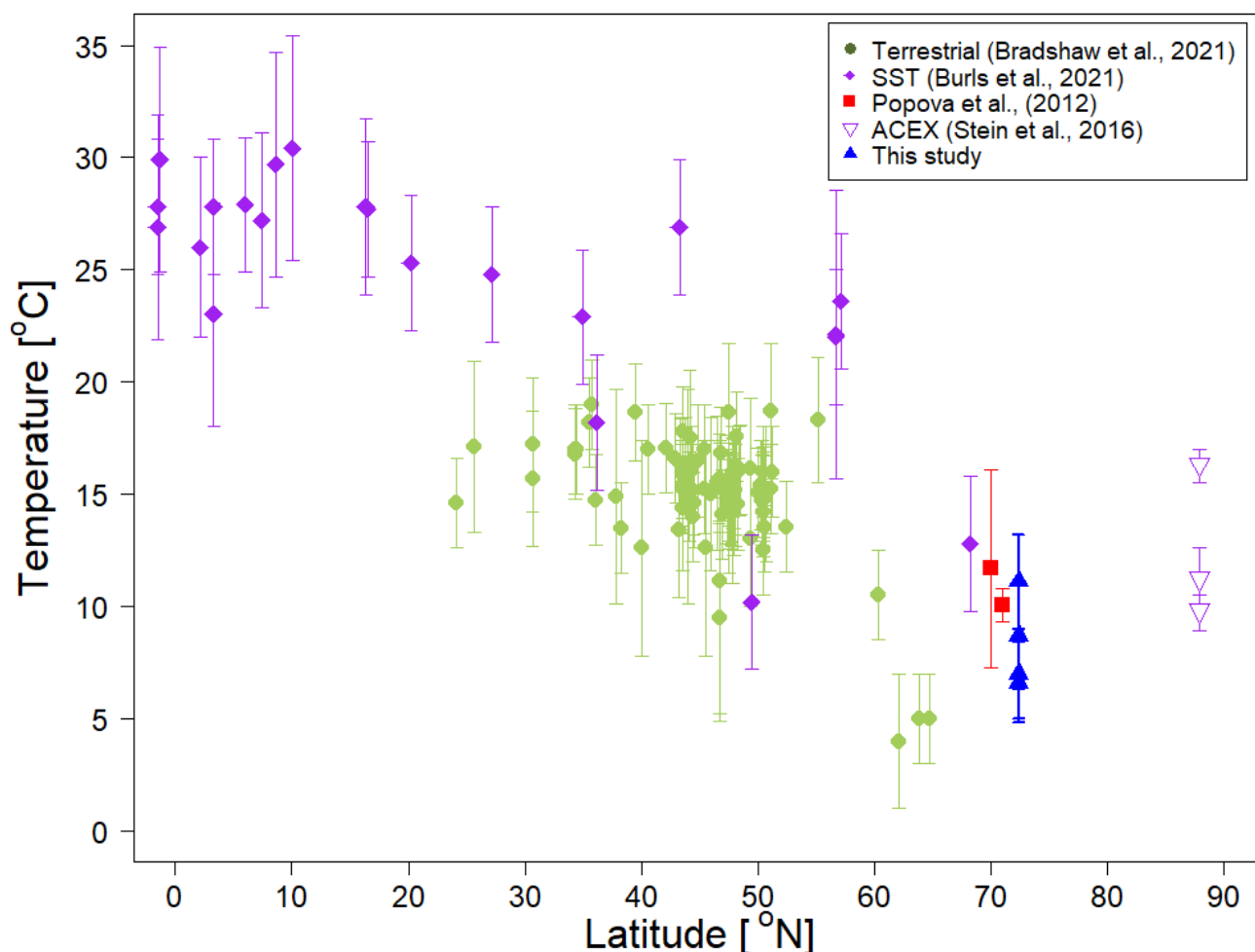
Figure 4: Compiled Northern Hemisphere late Miocene temperature reconstructions. Green circles are Tortonian terrestrial mean annual temperatures reconstructions from the Bradshaw et al. (2012) database with additional sites Temmirdekh-khaj and Omoloy from Popova et al. (2012) shown as red squares. Error bars for terrestrial reconstructions show minimum and maximum estimates. The late Miocene SST dataset from Burls et al. (2021) is shown as purple diamonds with error bars showing uncertainty in reconstruction estimate. Additional SST estimates from the ACEX borehole are shown as purple triangles (Stein et al., 2016). ACEX borehole temperatures show the average of the four different Alkenone derived temperature calibrations quoted in Stein et al. (2016), with error bars showing the maximum, and minimum values. Both terrestrial and SST datasets have been filtered to show only data with age uncertainties overlapping our Taba Bastaakh estimates. The blue triangles are the four Taba Bastaakh clumped isotope temperature reconstructions from this study.

To our knowledge, the Taba Bastaakh temperature reconstructions are the most northerly terrestrial Tortonian MAAT estimates to date and support the consensus of a reduced latitudinal temperature gradient during the late Miocene (Burls et al., 2021; Gaskell et al., 2022). Our temperature estimates agree well with independent high latitude temperature reconstructions (Fig.

4). Late Miocene fossil pollen assemblages from nearby sites Temmirdekh-khaj (132°E, 71°N) and Omoloy (133°E, 70°N) (Fig. 1) yield MAAT estimates between 7.3 and 16.1°C (Popova et al., 2012). The same authors infer a late Miocene MAAT of 9.7°C for the whole of eastern Siberia. Exceptionally high summer SSTs between 10 and 16°C have been reconstructed for the Arctic Ocean at the Lomonosov Ridge (88.5°N) (Stein et al., 2016). Our temperature reconstructions provide new evidence of a ca. 18 to 23°C warmer terrestrial Arctic during the Tortonian, at a time when global mean temperature was ca. 4.5°C warmer than pre-industrial (Pound et al., 2011). This Arctic amplification estimate is considerably higher than existing model projections of ca. 10 - 12°C Arctic warming by the end of the century under high emissions scenarios (Nazarenko et al., 2022; Xie et al., 2022).

5.2 Stable oxygen isotope records

Both Taba Bastaakh speleothem $\delta^{18}O$ records show very negative values (means: -15.6 ‰ and -16.9 ‰). Modern studies have shown that dripwater $\delta^{18}O$ ($\delta^{18}O_{dw}$) predominantly reflects changes in $\delta^{18}O$ of precipitation ($\delta^{18}O_p$) above a cave (Baker et al., 2019) which, at high latitudes, is largely driven by temperature (Dansgaard, 1964). Monthly mean values of $\delta^{18}O_p$ from both the Samoylov Island Research Station (2013-2017) and Tiksi (2004-2017) are highly correlated to mean monthly air temperatures (Spors, 2018). Thus, we interpret $\delta^{18}O_p$, and in turn $\delta^{18}O_{dw}$ and speleothem $\delta^{18}O$, as indicative of temperature variations at Taba Bastaakh.

Similarly negative $\delta^{18}O$ values (ca. -16 to -11 ‰) are found in Greenland speleothems during MIS 15a – 14 (Moseley et al., 2021), a middle-Pleistocene period of unusually warm and prolonged interglacials (Rodrigues et al., 2011; Hao et al., 2015). Holocene Arctic speleothem reconstructions are absent from the literature; however, the Taba Bastaakh isotope records agree well with modern Holocene values found in central Siberia 15-20 degrees latitude further south at Botovskaya Cave (55°N), Okhotnichya Cave (52°N) (ca. -18 to -13 ‰) (Lechleitner et al., 2020), and Kinderlinskaya Cave (54 °N) (ca. -14 to - 11 ‰) (Baker et al., 2017). Thus, the stable oxygen isotope records from Taba Bastaakh support the independent temperature estimates, suggesting much higher MAAT during the Tortonian than at present.

5.3 $\delta^{18}O$ signal of palaeo-dripwater

We estimate $\delta^{18}O_{dw}$ by using the clumped isotope derived temperatures in the temperature dependent water-calcite oxygen isotopic fractionation relationship from Tremaine et al. (2011) (Table 3). Given the control of $\delta^{18}O_p$ on $\delta^{18}O_{dw}$, the latter provides an estimate for $\delta^{18}O_P$. Due to the large sample sizes required for clumped isotope analysis, the samples integrate multiple growth layers and therefore $\delta^{18}O_{dw}$ values reflect multi-annual means.

$\delta^{18}O_{dw}$ ranges between -17.6 ± 0.4 ‰ and -18.4 ± 0.4 ‰ (VSMOW), within error of the fluid inclusion measurement from STBB I – 1 (-17.5 ± 1.0 ‰). Agreement between these two independent $\delta^{18}O_{dw}$ derivations provides additional confidence in

our estimate. We stress that this assessment does not consider the influence of additional post-precipitation evaporative processes that complicate isolation of a pure precipitation signal from speleothem fluid inclusions (Lachniet, 2009).

360

Our reconstructed Lena Delta $\delta^{18}O_p$ values for the Tortonian suggest a mean annual precipitation regime between the modern summer (-15.9 ‰) and autumnal regimes (-19.1 ‰) (modern annual mean = -21.6 ‰) (Bonne et al., 2020) .

Table 3: Dripwater isotopic composition estimates for the four Taba Bastaakh speleothems. $\delta^{18}O_{cc}$ is the $\delta^{18}O$ of calcium carbonate.
365 **$\delta^{18}O_{cc}$ uncertainties are standard errors. $\delta^{18}O_{dw}$ uncertainty is calculated from propagation of $T_{\Delta47}$ and $\delta^{18}O_{CC}$ uncertainties.**

Sample	$T_{\Delta47}$ (°C)	$\delta^{18}O_{cc}$ (‰, VPDB)	$\delta^{18}O_{dw}$ (‰, VSMOW)	$\delta^{18}O_{FI}$ (‰, VSMOW)
STBB I - 1	11.1 ± 2.1	-16.02 ± 0.01	-17.6 ± 0.4	-17.5 ± 1.0
STBB II - 7	6.6 ± 1.8	-15.86 ± 0.01	-18.3 ± 0.4	
STBB 4-2	7.0 ± 2.0	-16.01 ± 0.01	-18.4 ± 0.4	
STBB 4 - 3	8.7 ± 2.4	-15.87 ± 0.01	-17.9 ± 0.5	

5.4 Seasonal hydrological regime

We propose that the cyclical behaviour of trace elements is driven by a strong seasonal hydrological regime at the time of speleothem deposition. The identified hydrological PC groups in both STBB I – 1 (PC1) and STBB II – 7 (PC2) are associated
370 with element ratios widely utilised as hydrological proxies: most commonly Mg/Ca, Sr/Ca and Ba/Ca (e.g., Tooth & Fairchild, 2003; Treble et al., 2015). Correlation of Sr and Mg is often used as an indicator of prior carbonate precipitation (PCP) from infiltration waters before they reach the speleothem formation site (Wassenburg et al., 2020). Sr/Ca and Mg/Ca exhibit no consistent relationship in either Taba Bastaakh sample, with periods of high correlation interspersed with periods of no correlation (Fig. S4). Deviation from constant Mg/Ca vs Sr/Ca ratios can arise from growth rate variability (Sliwinski et al.,
375 2023) and changing mixing ratios of dripwater solutions derived from multiple geological endmembers (Tremaine & Froelich, 2013). Dating constraints hinder identification of growth rate variability in the Taba Bastaakh records, however Sr/Ca and Mg/Ca decoupling could arise from periods of hydrological rerouting or changing endmember dissolution rates between the carbonate and the overlying dolomitic limestone (Izokh & Yazikov, 2017) altering Mg/Ca concentration input.
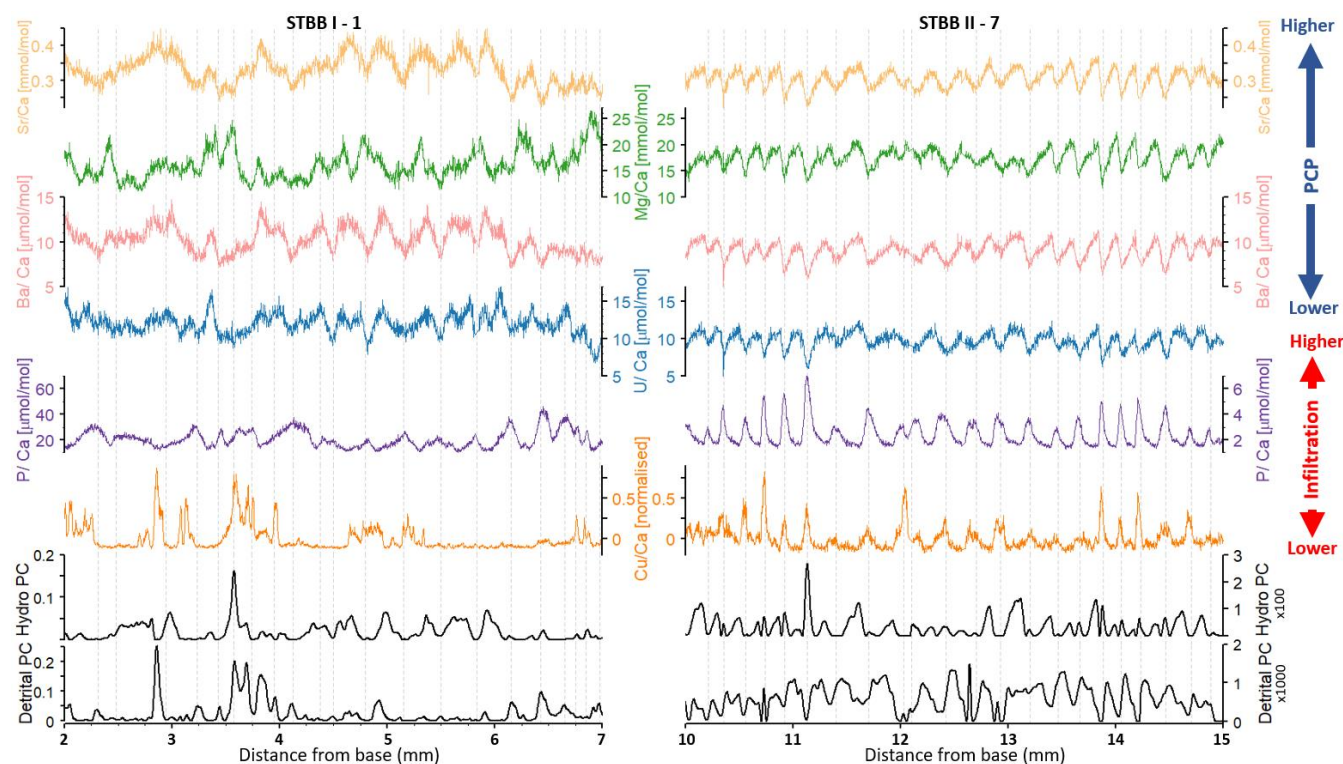
Figure 5: High resolution trace element concentrations, and major principal components along the STBB I – 1 and STBB II – 7 sampling profiles. Cu/Ca ratio has been mean-normalised for easier comparison between the two samples. Grey dashed vertical lines mark the positions of Sr/Ca troughs.

Tremaine and Froelich (2013) showed that in order to diagnose Mg/Ca and Sr/Ca as reliable 'wet vs. dry' proxies, Sr/Mg must remain constant along the entire sampling profile. Whilst this is not the case in the Taba Bastaakh records, Sr/Ca is remarkably highly correlated with Ba/Ca and U/Ca along the entire growth length of both Taba Bastaakh samples (Figs. S3 and S4). Ba/Ca has been extensively utilised as a PCP proxy (e.g., Wassenburg et al., 2012 ; Stoll et al., 2012) and might constitute a more robust PCP proxy that is less likely affected by host rock composition at Taba Bastaakh. Fewer studies have considered U/Ca as potential indicator of infiltration changes. Dripwater U is derived from bedrock dissolution and is readily incorporated into the calcite lattice (Oster et al., 2023) . The strong correlation of U with both Sr and Ba in the Taba Bastaakh records suggests that U/Ca may also reflect changes in PCP in the Taba Bastaakh records. Finally, P/Ca is also included in the hydrological principal component in STBB I - 1, and is strongly anticorrelated with Sr, Ba, and U. P is scavenged from infiltration water during calcite precipitation, thus decreasing P/Ca in dripwater during periods of elevated PCP (Johnson et al., 2006) — as is observed in the Taba Bastaakh records (indicated by elevated Sr/Ca, Ba/Ca and U/Ca, Fig. 5).

The detrital principal component is characterised by metals which are commonly associated with organic matter flux into the cave (Hartland et al., 2012). These metals are poorly soluble and colloidally transported through organic matter binding during

soil infiltration (Hartland et al., 2012). Hartland et al. (2012) demonstrated Cu and Co organic binding by showing speleothem Cu/Ca vs Co/Ca ratios in line with those predicted based on n1 NICA-Donnan humic and fulvic binding affinity ratios (Milne

400 et al., 2003). We repeat this calculation for our records and find that the measured Cu/Ca vs Co/Ca ratios show good agreement with predicted ratios in STBB II – 7 (Fig. S5), confirming these metals are indeed derived from organic binding in this sample. There is poor agreement between predicted and measured ratios in STBB I – 1 suggesting detrital metals in this sample are not associated with organic binding. Phosphorus is also included in the detrital principal component in STBB II – 7. P supply has been linked with vegetative leaching during storm events (Poinke el al., 1997) with maximum P/Ca linked to elevated

405 infiltration rates (Borsato et al., 2007). Thus, the strong positive correlation observed between P and organically binded metals provides further evidence that these element variations are reflecting infiltration rates in STBB II – 7.

We present a subsection of the trace element records in Fig. 5 where correlation between Mg and other hydrological proxies is highest to illustrate the relationship between hydrological and detrital proxies. In STBB II – 7, maxima in PCP controlled

410 elements Sr, Mg, Ba and U coincide with minima in the infiltration-controlled elements P and Cu. Thus, wet seasons are identified as maxima in infiltration proxies (Cu/Ca and P/Ca), and minima in the PCP proxies Sr, Mg, Ba, and U. The opposite is true for dry seasons. The relationship between detrital infiltration and PCP proxies is less apparent in STBB I – 1 (Fig. 5), where we have demonstrated that detrital proxies are not controlled by organic matter influx (Fig. S5). However, strong cyclicity is observed in all PCP proxies, as well as P, which shows a similar anticorrelation with PCP proxies as in STBB II –

415 7.

Spectral analysis displays dominant trace element cycles of 0.3 and 0.5 mm and 0.2 mm in STBB I – 1 and STBB II – 7 respectively (Fig. S6). Our assertion that these cycles are annual is supported by the observed alignment of the Sr/Ca record with annual banding in STBB II – 7 (Fig. S7), identified by changes in the visual greyscale. We use the free ImageJ software

420 to extract greyvalues (the intensity of light carried in a single pixel) along the growth length of a high-resolution composite image STBB II – 7 thin sections (Breitenbach & Marwan, 2023). In this way, annual growth bands were identified. Sr/Ca peaks coincide with greyscale peaks (brighter layers). Thus, our trace element periods reflect growth rates of 200 µm (STBB II - 7) and 300 µm (STBB I -1) a year, similar to those observed in modern temperate regions (Johnson et al., 2006; Sherwin & Baldini, 2011).

425

We compare Miocene and modern-day hydrological seasonality using a 20-year instrumental record of precipitation from the nearby Samoylov Island Research Station. We combined common hydrological proxies Sr/Ca, Ba/Ca, U/Ca, Mg/Ca, and P/Ca to obtain a single representative proxy-stack-average timeseries and aligned it to the instrumental record using dynamic time warping (Berndt & Clifford, 1994) (See SOM for details, Fig. S8). While this methodology does not eliminate the considerable

430 challenges of comparing palaeoseasonal proxy data to modern seasonality, it yields a pseudo-seasonal time axis that allows us to estimate precipitation seasonality in a comparable fashion for both sets of records. We compared the aligned modern and

Miocene hydrological seasons using a spectral seasonality measure. Precipitation seasonality is quantified by the total spectral power $|P|_s$ summed over the spectral band that closely encapsulates the seasonal peak (Fig. S9). Higher power in the seasonal band is interpreted as a more pronounced/stable seasonal signal. Detailed methodology is given in the supplementary materials.

435   The combined hydrological proxy records suggest a stronger seasonal precipitation regime during the Tortonian (i.e. a more pronounced seasonal cycle) compared with modern day conditions (Fig. 6). This is true of both samples, with significantly higher median spectral power in the seasonal band in the Miocene compared with the modern.
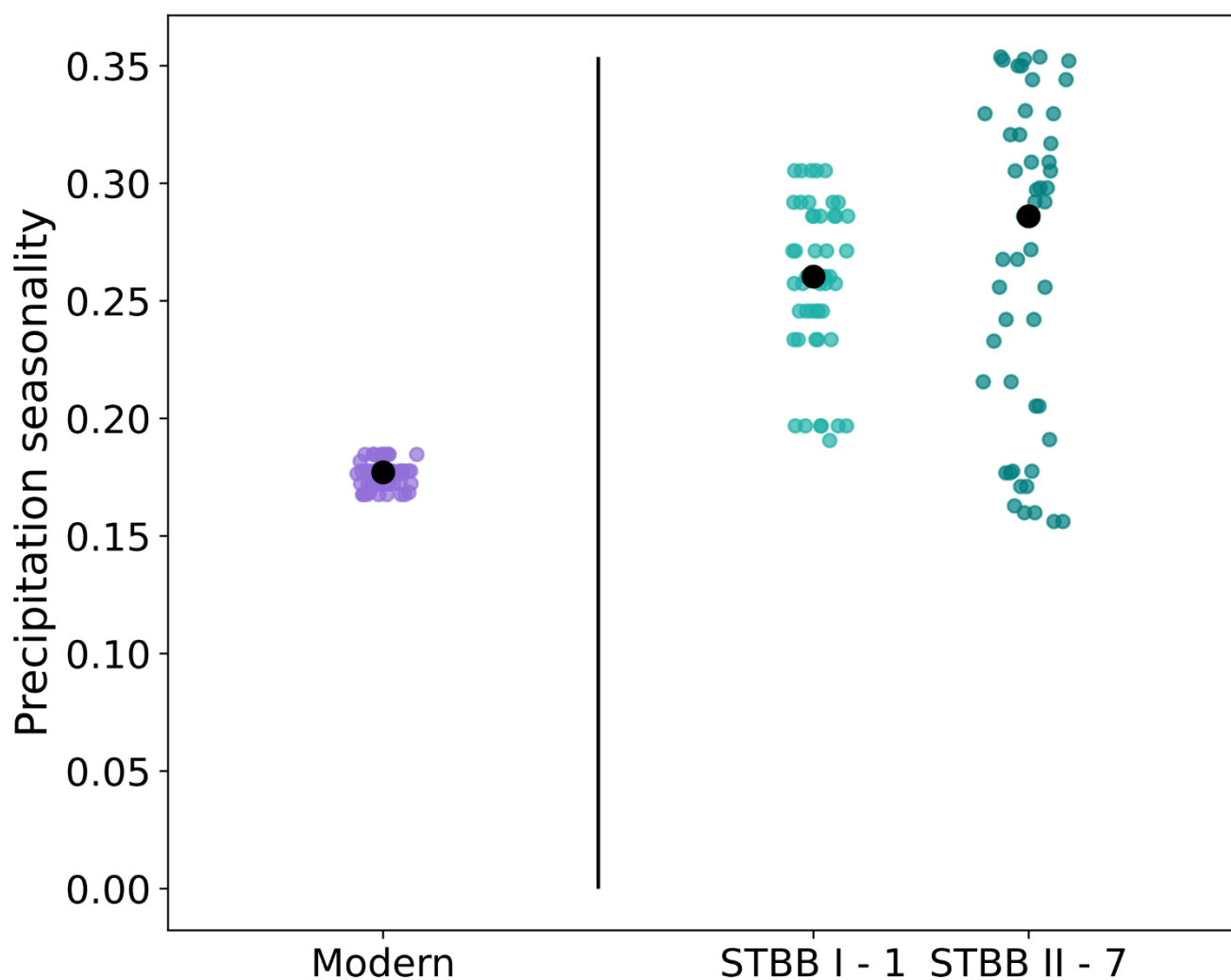
Figure 6: Reconstructed precipitation seasonality ($|P|_s$ summed over the seaonal peak spectral band) in Tortonian samples STBB I - 1 and STBB II - 7, compared with the modern day. An alignment procedure based on dynamic time warping allows for their comparison. Coloured points show seasonality values for different widths of the seasonal band between 0.2 (0.9 - 1.1) and 0.5 (0.75 - 1.25). Black points show the median over all values. Both samples show overall enhanced seasonality in the Miocene compared with the modern day.

445

Numerous studies have suggested the Miocene was a time of enhanced seasonality in the mid latitudes with warm-wet, cold-dry seasonal cycles in central Europe (Bruch et al., 2011; Harzhauser et al., 2011). At high latitudes, the picture is less conclusive. Pollen reconstructions from eastern Siberia suggest the late Miocene marks the onset of modern atmospheric circulation patterns and the establishment of today's wet summer/dry winter regime (Popova et al., 2012). At Temmirdekh-

450 khaj and Omoloy, Miocene pollen reconstructions suggest the mean annual range in precipitation (the difference between wet and dry season amplitude) was 70 - 80 mm and 110 - 130 mm respectively. This seems large compared with today's mean annual precipitation of 169 mm but should be viewed in context of a likely wetter Tortonian regime given higher moisture availability from a summer ice-free Arctic (Stein et al., 2016). Analysis of fossil wood δ^{13}C from Cherskiy (N67.7˚, E161.6˚) in northeastern Siberia shows a high variability in precipitation, with the wet season alternating between summer and winter

455 (Schubert et al., 2017). In contrast, our Taba Bastaakh records suggest an enhanced seasonal precipitation regime compared with the modern day. We propose this likely arose from differing moisture availability from the nearby Arctic Ocean which was largely sea-ice covered during the Tortonian winter and ice-free during Tortonian summers (Stein et al., 2016). This would have led to enhanced evaporation and moisture transport into northern Siberia in the summer, compared with winter. This effect appears to outweigh any impact of reduced continentality given global average sea levels ca. 10 m higher during the late

460 Miocene compared with modern (Miller et al., 2005). A likely return to similar ice coverage over the coming century (Sigmond et al., 2018) may drive a shift to more enhanced seasonal precipitation regimes similar to those we infer for the Tortonian.

5.5 Near-future Arctic climate and implications for permafrost thaw

Observational evidence suggests that annual and extreme precipitation is already increasing in permafrost regions (Wang et al., 2021) and driving permafrost thaw in the Lena River basin (Iijima et al., 2010). Whilst we are unable to quantify

465 precipitation amount from our data, the enhanced precipitation volatility inferred for the Tortonian suggests annual and extreme precipitation will continue to increase given MAAT rises similar to those we infer for the Miocene and reduced sea-ice cover in the Arctic Ocean. This will likely further destabilise permafrost as extreme precipitation events increase soil moisture and, in turn, the latent heat of freezing (Iijima et al., 2010).

470 Our speleothem records suggest a significantly warmer climate in the high Arctic during the Tortonian, with MAAT 18.9-23.4°C warmer than present. Globally, Tortonian climate was similar to the end of the century projections under high emissions scenarios which predict between 2 – 5°C of warming (Masson-Delmotte et al., 2021). Global mean annual temperatures were some 4.5°C warmer than pre-industrial (Pound et al., 2011) and atmospheric carbon dioxide concentrations up to 600 ppm (Rae et al., 2021).. Thus, our findings provide estimates for end-of-century Arctic temperature amplification and precipitation

475 variability under high emissions scenarios. Our estimate is considerably higher than reconstructions for the middle-Pliocene Warm Period (3.3 - 3.0 Ma) which suggested Arctic warming of 7.2°C given global mean temperatures 3.2°C above pre-industrial (de Nooijer et al., 2020).
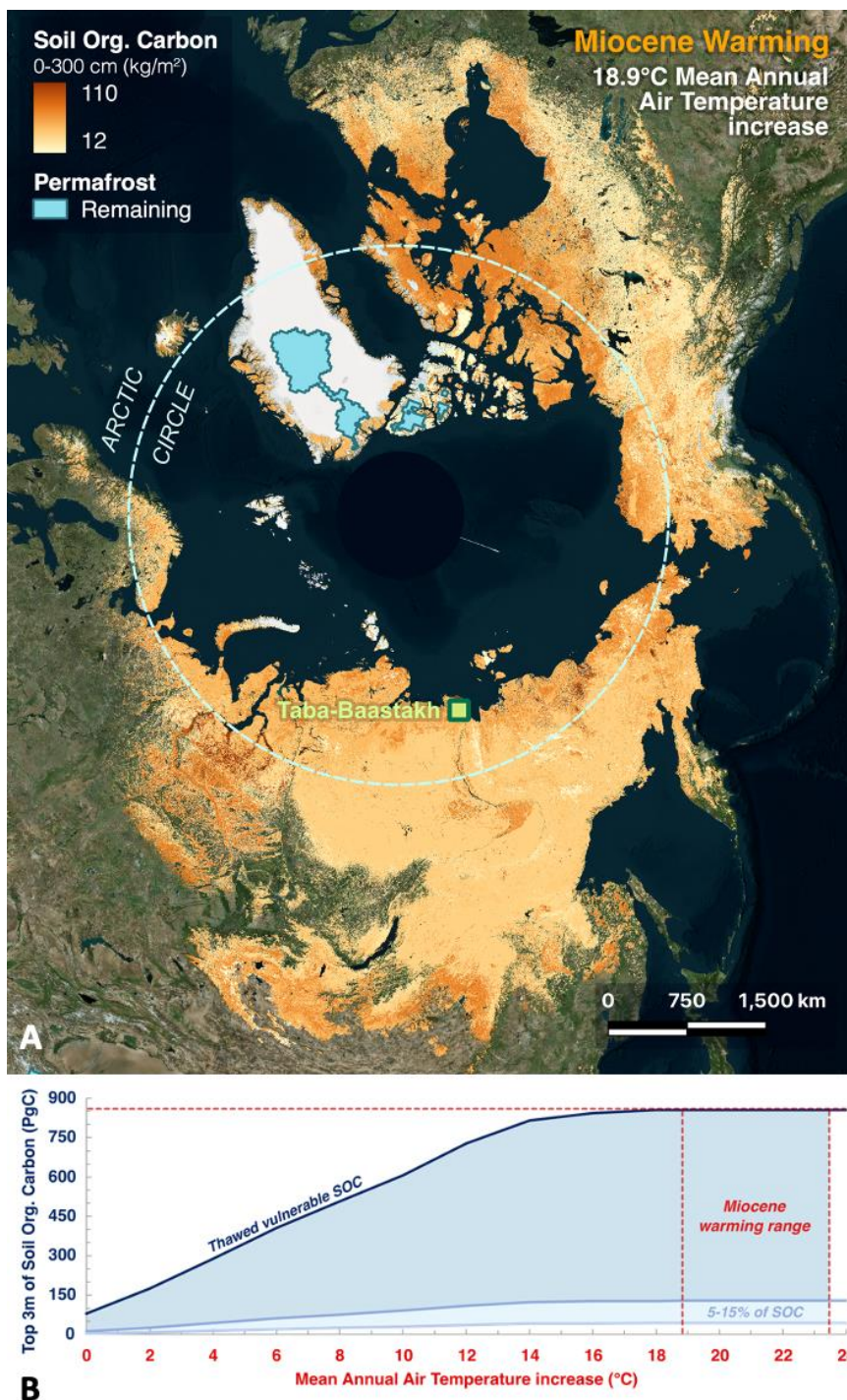
**Figure 7: (A) Modern SOC for 0-3 m (Palmtag et al., 2022) is mapped for the area vulnerable to thaw given an 18.9°C temperature
increase (MAAT = 6.6 °C – our lower $T_{\Delta47}$ estimate (updated from Vaks et al., in review). (B) Graph depicts the total soil organic
carbon (PgC) vulnerable to thaw given various MAAT increase scenarios, with 5-15% likely to release as greenhouse gas emissions
on a short-term timescale.**

Today, the Lena Delta region sits at the northern Eurasian terrestrial permafrost boundary and is underlain by deep, continuous
485 permafrost of 400 – 600 m thickness (Boike et al., 2019) . Arctic amplification of a magnitude similar to that reconstructed for
the Tortonian would threaten the stability of permafrost across the entire Eurasian landmass, driving further carbon emissions
in a positive feedback cycle. Evidence from ice-wedge pseudomorphs suggests the onset of high-latitude Northern Hemisphere
permafrost formation occurred in the late Pliocene (~3 Ma) (Opel et al., 2024) and it is very likely that the Northern Hemisphere
was permafrost-free during the Tortonian (Vaks et al., in review).

490

Using our new temperature reconstructions, we estimate total potential permafrost derived carbon emissions given future
warming similar to that reconstructed for the Tortonian and update the previous calculation from Vaks et al. (in review). These
authors used the presence of speleothems alone to derive a more conservative (lower) Taba Bastaakh temperature limit of -
5°C. Here we repeat their calculation using our upper and lower temperature estimates of ~6.6°C and 11.1°C, which amounts
495 to an 18.9−23.4°C increase from the present-day MAAT of -12.3°C. We calculate carbon emissions by overlaying vulnerable
permafrost regions with a soil organic carbon (SOC) model (Palmtag et al., 2022) for the upper 3 metres of permafrost soil.
Even considering a conservative permafrost boundary of MAAT = 0°C (often, colder temperatures down to MAAT = -8°C are
required to sustain continuous permafrost), the warming by 18.9-23.4°C would thaw virtually all permafrost. With such levels
of Arctic warming, 98-100 % of Northern Hemisphere permafrost area would be vulnerable to near-surface thaw (Fig. 7). This
500 is slightly higher than recent middle-Pliocene estimates from Guo et al. (2023), who found a 93 ± 3% decrease in permafrost
extent based on a ca. 7.2°C warmer Arctic compared with pre-industrial temperatures. Based on Palmtag et al. (2022), which
excludes the Tibetan Plateau region, we estimate at least 855 PgC is contained in permafrost that is vulnerable to thaw in the
underlying 3 metres of soil. Of this, 5−15% (43−128 PgC) would likely be released to the atmosphere within decades (Schuur
et al., 2022), while longer term emissions remain uncertain as new, expanding vegetation regimes stabilise and thawed regions
505 either dry out or continue to sequester carbon as active wetlands.

Our estimate provides a first approximation of potential permafrost emissions by 2100 given global temperature rises similar
to those projected by the end of century under high carbon emissions (Masson-Delmotte et al., 2021). We stress that our
calculation assumes a constant 18.9 – 23.4°C temperature rise across all permafrost regions (equal to the reconstructed
510 Tortonian temperature range at Taba Bastaakh) and undoubtedly simplifies spatial variability in warming. However, our
findings suggest that permafrost thaw will contribute significantly to future carbon emissions, and we highlight the importance
of including permafrost feedbacks in quantifying future emissions budgets.

6 Conclusions

515 We present the first speleothem derived temperature and precipitation seasonality records from Arctic Siberia during the Tortonian (11.63 – 7.246 Ma). Our findings offer insight into high latitude climate during a period when the global mean surface temperature was similar to that projected over the coming decades under high emission scenarios.

Apparent hydrologically driven element cycles suggest a more seasonal precipitation regime compared with the modern day,
520 likely driven by fluctuations in Arctic Sea ice extent. Given probable reductions in summer Arctic ice extent over the coming decades, a return to more volatile precipitation regimes seems likely, with increased summer precipitation driving permafrost thaw and impacting local infrastructure.

We use two independent methodologies to reconstruct Tortonian temperatures between 6.6 and 11.8°C from high latitude
525 central Siberia. These findings are in good agreement with previous estimates from the region and support the consensus of a substantially warmer late Miocene climate compared with modern day. Our findings provide much needed estimates for future Arctic amplification, implying Arctic MAAT increases of 18.9−23.4°C above modern, given global mean temperature rises of ca. 4.5°C above pre-industrial−considerably higher than current estimates from climate models.

530 Amplified Arctic warming implied by our study would render the majority of Arctic and sub-Arctic surface permafrost free, resulting in an additional estimated 43-128 Pg of carbon emissions. This highlights the significant contribution of permafrost feedbacks to future emissions and the urgent need to incorporate them into future carbon budget calculations.

Author contributions

SU and SB conceptualised the study. AV, OS, AK, IA, and SB were responsible for sample collection. AV and GH provided
535 U-Pb dating of samples. SU and SM performed clumped isotope analysis. FL and SU milled samples and performed stable isotope analysis. PS performed trace element analysis. YD performed fluid inclusion measurements. TB and AG contributed to interpretation of the dataset, with TB providing the comparison between Miocene and modern seasonal cycles (and production of figures 6, S8 and S9), and AG responsible for calculating likely future emissions from permafrost (and production of figure 7). SU oversaw writing of the manuscript and figure preparation, with significant input from FL, TO, SB,
540 and AG. All authors contributed to the review and editing of the manuscript.

Competing Interests

The authors declare that they have no conflict of interest.

Data availability statement

All data will be included in this manuscript in the supporting information. Trace element, stable, and clumped isotope data
545   will be archived in the PANGAEA database pending acceptance of this manuscript.

Disclaimer

Any use of trade, firm, or product names is for descriptive purposes only and does not imply endorsement by the U.S.
Government.

Acknowledgements

550   The authors would like to thank the Leverhulme Trust (RPG-2020-334), Natural Environment Research Council
(NE/KE005057/1 awarded to A. Vaks), and Swiss National Science Foundation (grant P2EZP2_172213 awarded to F.
Lechleitner) who funded this research. We thank Birgit Schröder at GFZ Potsdam for providing the Plessen internal standard
used in our stable isotope measurements and Paul Dennis and Norbert Marwan for acting as independent reviewers of the draft
manuscript. TB acknowledges fruitful discussions with Norbert Marwan.

555   **References**

Anderson, N. T., Kelson, J. R., Kele, S., Daëron, M., Bonifacie, M., Horita, J., Mackey, T. J., John, C. M., Kluge, T., Petschnig,
P., Jost, A. B., Huntington, K. W., Bernasconi, S. M., & Bergmann, K. D. (2021). A Unified Clumped Isotope
Thermometer Calibration (0.5–1,100°C) Using Carbonate-Based Standardization. *Geophysical Research Letters*, *48*(7).
https://doi.org/10.1029/2020GL092069
560   Baker, A., Hartmann, A., Duan, W., Hankin, S., Comas-Bru, L., Cuthbert, M. O., Treble, P. C., Banner, J., Genty, D., Baldini,
L. M., Bartolomé, M., Moreno, A., Pérez-Mejías, C., & Werner, M. (2019). Global analysis reveals climatic controls on
the oxygen isotope composition of cave drip water. *Nature Communications*, *10*(1). https://doi.org/10.1038/s41467-019-
11027-w
Baker, J. L., Lachniet, M. S., Chervyatsova, O., Asmerom, Y., & Polyak, V. J. (2017). Holocene warming in western
565   continental Eurasia driven by glacial retreat and greenhouse forcing. *Nature Geoscience*, *10*(6), 430–435.
https://doi.org/10.1038/ngeo2953
Bernasconi, S. M., Daëron, M., Bergmann, K. D., Bonifacie, M., Meckler, A. N., Affek, H. P., Anderson, N., Bajnai, D.,
Barkan, E., Beverly, E., Blamart, D., Burgener, L., Calmels, D., Chaduteau, C., Clog, M., Davidheiser-Kroll, B., Davies,
A., Dux, F., Eiler, J., … Ziegler, M. (2021). InterCarb: A Community Effort to Improve Interlaboratory Standardization

570   of the Carbonate Clumped Isotope Thermometer Using Carbonate Standards. *Geochemistry, Geophysics, Geosystems*, *22*(5). https://doi.org/10.1029/2020GC009588

Bernasconi, S. M., Müller, I. A., Bergmann, K. D., & Breitenbach, S. F. M. (2018). *Reducing Uncertainties in Carbonate Clumped Isotope Analysis Through Consistent Carbonate-Based Standardization Geochemistry, Geophysics, Geosystems*. 2895–2914. https://doi.org/10.1029/2017GC007385

575 Berndt, D. J., & Clifford, J. (1994). Using dynamic time warping to find patterns in time series. *Proceedings of the 3rd International Conference on Knowledge Discovery and Data Mining*, 359–370.

Bintanja, R., Van Der Wiel, K., Van Der Linden, E. C., Reusen, J., Bogerd, L., Krikken, F., & Selten, F. M. (2020). Strong future increases in Arctic precipitation variability linked to poleward moisture transport. In *Sci. Adv* (Vol. 6).

Biskaborn, B. K., Smith, S. L., Noetzli, J., Matthes, H., Vieira, G., Streletskiy, D. A., Schoeneich, P., Romanovsky, V. E.,
580   Lewkowicz, A. G., Abramov, A., Allard, M., Boike, J., Cable, W. L., Christiansen, H. H., Delaloye, R., Diekmann, B., Drozdov, D., Etzelmüller, B., Grosse, G., Lantuit, H. (2019). Permafrost is warming at a global scale. *Nature Communications*, *10*(1). https://doi.org/10.1038/s41467-018-08240-4

Boike, J., Kattenstroth, B., Abramova, K., Bornemann, N., Chetverova, A., Fedorova, I., Fröb, K., Grigoriev, M., Grüber, M., Kutzbach, L., Langer, M., Minke, M., Muster, S., Piel, K., Pfeiffer, E. M., Stoof, G., Westermann, S., Wischnewski, K.,
585   Wille, C., & Hubberten, H. W. (2013). Baseline characteristics of climate, permafrost and land cover from a new permafrost observatory in the Lena River Delta, Siberia (1998-2011). *Biogeosciences*, *10*(3), 2105–2128. https://doi.org/10.5194/bg-10-2105-2013

Boike, J., Nitzbon, J., Anders, K., Grigoriev, M., Bolshiyanov, D., Langer, M., Lange, S., Bornemann, N., Morgenstern, A., Schreiber, P., Wille, C., Chadburn, S., Gouttevin, I., Burke, E., & Kutzbach, L. (2019). A 16-year record (2002-2017)
590   of permafrost, active-layer, and meteorological conditions at the Samoylov Island Arctic permafrost research site, Lena River delta, northern Siberia: An opportunity to validate remote-sensing data and land surface, snow, and permafrost models. *Earth System Science Data*, *11*(1), 261–299. https://doi.org/10.5194/essd-11-261-2019

Bonne, J. L., Meyer, H., Behrens, M., Boike, J., Kipfstuhl, S., Rabe, B., Schmidt, T., Schönicke, L., Steen-Larsen, H. C., & Werner, M. (2020). Moisture origin as a driver of temporal variabilities of the water vapour isotopic composition in the
595   Lena River Delta, Siberia. *Atmospheric Chemistry and Physics*, *20*(17), 10493–10511. https://doi.org/10.5194/acp-20-10493-2020

Borsato, A., Frisia, S., Fairchild, I. J., Somogyi, A., & Susini, J. (2007). Trace element distribution in annual stalagmite laminae mapped by micrometer-resolution X-ray fluorescence: Implications for incorporation of environmentally significant species. *Geochimica et Cosmochimica Acta*, *71*(6), 1494–1512. https://doi.org/10.1016/j.gca.2006.12.016

600 Bradshaw, C. D., Lunt, D. J., Flecker, R., Salzmann, U., Pound, M. J., Haywood, A. M., & Eronen, J. T. (2012). The relative roles of CO2 and palaeogeography in determining late Miocene climate: Results from a terrestrial model-data comparison. *Climate of the Past*, *8*(4), 1257–1285. https://doi.org/10.5194/cp-8-1257-2012

Brand, W. A., Assonov, S. S., & Coplen, T. B. (2010). Correction for the 17O interference in δ(13C) measurements when analyzing CO2 with stable isotope mass spectrometry (IUPAC Technical Report). *Pure and Applied Chemistry*, *82*(8), 1719–1733. https://doi.org/10.1351/PAC-REP-09-01-05

Breitenbach, S. F. M., & Marwan, N. (2023). Acquisition and analysis of greyscale data from stalagmites using ImageJ software, *Cave and Karst Science*. (Vol. 50, Issue 2).

Bruch, A. A., Utescher, T., & Mosbrugger, V. (2011). Precipitation patterns in the Miocene of Central Europe and the development of continentality. *Palaeogeography, Palaeoclimatology, Palaeoecology*, *304*(3–4), 202–211. https://doi.org/10.1016/j.palaeo.2010.10.002

Burls, N. J., Bradshaw, C. D., De Boer, A. M., Herold, N., Huber, M., Pound, M., Donnadieu, Y., Farnsworth, A., Frigola, A., Gasson, E., von der Heydt, A. S., Hutchinson, D. K., Knorr, G., Lawrence, K. T., Lear, C. H., Li, X., Lohmann, G., Lunt, D. J., Marzocchi, A., … Zhang, Z. (2021). Simulating Miocene Warmth: Insights From an Opportunistic Multi-Model Ensemble (MioMIP1). *Paleoceanography and Paleoclimatology*, *36*(5). https://doi.org/10.1029/2020PA004054

Chylek, P., Folland, C., Klett, J. D., Wang, M., Hengartner, N., Lesins, G., & Dubey, M. K. (2022). Annual Mean Arctic Amplification 1970–2020: Observed and Simulated by CMIP6 Climate Models. *Geophysical Research Letters*, *49*(13). https://doi.org/10.1029/2022GL099371

Coplen, T. B. (2007). Calibration of the calcite–water oxygen-isotope geothermometer at Devils Hole, Nevada, a natural laboratory. *Geochimica et Cosmochimica Acta*, *71*(16), 3948–3957. https://doi.org/10.1016/j.gca.2007.05.028

Craig, H. (1961). Isotopic variations in meteoric waters. *Science*, *133*(3465), 1702–1703. https://doi.org/10.1126/science.133.3465.1702

Daëron, M., Blamart, D., Peral, M., & Affek, H. P. (2016). Absolute isotopic abundance ratios and the accuracy of Δ47 measurements. *Chemical Geology*, *442*, 83–96. https://doi.org/10.1016/j.chemgeo.2016.08.014

Daëron, M., & Gray, W. R. (2023). Revisiting Oxygen-18 and Clumped Isotopes in Planktic and Benthic Foraminifera. *Paleoceanography and Paleoclimatology*, *38*(10). https://doi.org/10.1029/2023PA004660

Damon Matthews, H., Tokarska, K. B., Rogelj, J., Smith, C. J., MacDougall, A. H., Haustein, K., Mengis, N., Sippel, S., Forster, P. M., & Knutti, R. (2021). An integrated approach to quantifying uncertainties in the remaining carbon budget. *Communications Earth and Environment*, *2*(1). https://doi.org/10.1038/s43247-020-00064-9

Dansgaard, W. (1964). Stable isotopes in precipitation. *Tellus, 16*(4), 436–468. https://doi.org/10.3402/tellusa.v16i4.8993

Dennis, K. J., Affek, H. P., Passey, B. H., Schrag, D. P., & Eiler, J. M. (2011). Defining an absolute reference frame for 'clumped' isotope studies of CO2. *Geochimica et Cosmochimica Acta*, *75*(22), 7117–7131. https://doi.org/10.1016/j.gca.2011.09.025

Dublyansky, Y. V., & Spötl, C. (2009). Hydrogen and oxygen isotopes of water from inclusions in minerals: Design of a new crushing system and on-line continous-flow isotope ratio mass spectrometric analysis. *Rapid Communications in Mass Spectrometry*, *23*(17), 2605–2613. https://doi.org/10.1002/rcm.4155

Eiler, J. M., & Schauble, E. (2004). 18O13C16O in Earth's atmosphere. *Geochimica et Cosmochimica Acta*, *68*(23), 4767–4777. https://doi.org/10.1016/j.gca.2004.05.035

Fan, Y., & van den Dool, H. (2008). A global monthly land surface air temperature analysis for 1948-present. *Journal of Geophysical Research Atmospheres*, *113*(1). https://doi.org/10.1029/2007JD008470

Farquharson, L. M., Romanovsky, V. E., Cable, W. L., Walker, D. A., Kokelj, S. V., & Nicolsky, D. (2019). Climate Change Drives Widespread and Rapid Thermokarst Development in Very Cold Permafrost in the Canadian High Arctic. *Geophysical Research Letters*, *46*(12), 6681–6689. https://doi.org/10.1029/2019GL082187

Fernandez, A., Müller, I. A., Rodríguez-Sanz, L., van Dijk, J., Looser, N., & Bernasconi, S. M. (2017). A Reassessment of the Precision of Carbonate Clumped Isotope Measurements: Implications for Calibrations and Paleoclimate Reconstructions. *Geochemistry, Geophysics, Geosystems*, *18*(12), 4375–4386. https://doi.org/10.1002/2017GC007106

Finestone, E. M., Breeze, P. S., Breitenbach, S. F. M., Drake, N., Bergmann, L., Maksudov, F., Muhammadiyev, A., Scott, P., Cai, Y., Khatsenovich, A. M., Rybin, E. P., Nehrke, G., Boivin, N., & Petraglia, M. (2022). Paleolithic occupation of arid Central Asia in the Middle Pleistocene. *PLoS ONE*, *17*. https://doi.org/10.1371/journal.pone.0273984

Froitzheim, N., Majka, J., & Zastrozhnov, D. (2021). Methane release from carbonate rock formations in the Siberian permafrost area during and after the 2020 heat wave. *Proceedings of the National Academy of Sciences of the United States of America*, *118*(32). https://doi.org/10.1073/pnas.2107632118

Gaskell, D. E., Huber, M., O'brien, C. L., Inglis, G. N., Acosta, R. P., Poulsen, C. J., & Hull, P. M. (2022). The latitudinal temperature gradient and its climate dependence as inferred from foraminiferal δ 18 O over the past 95 million years. *Proceedings of the National Academy of Sciences, 119*(11), 2111332119. https://doi.org/10.1073/pnas

Gasser, T., Kechiar, M., Ciais, P., Burke, E. J., Kleinen, T., Zhu, D., Huang, Y., Ekici, A., & Obersteiner, M. (2018). Path-dependent reductions in CO2 emission budgets caused by permafrost carbon release. *Nature Geoscience*, *11*(11), 830–835. https://doi.org/10.1038/s41561-018-0227-0

Hartland, A., Fairchild, I. J., Lead, J. R., Borsato, A., Baker, A., Frisia, S., & Baalousha, M. (2012). From soil to cave: Transport of trace metals by natural organic matter in karst dripwaters. *Chemical Geology*, *304–305*, 68–82. https://doi.org/10.1016/j.chemgeo.2012.01.032

Harzhauser, M., Piller, W. E., Müllegger, S., Grunert, P., & Micheels, A. (2011). Changing seasonality patterns in Central Europe from Miocene Climate Optimum to Miocene Climate Transition deduced from the Crassostrea isotope archive. *Global and Planetary Change*, *76*(1–2), 77–84. https://doi.org/10.1016/j.gloplacha.2010.12.003

Haywood, A. M., Tindall, J. C., Dowsett, H. J., Dolan, A. M., Foley, K. M., Hunter, S. J., Hill, D. J., Chan, W. Le, Abe-Ouchi, A., Stepanek, C., Lohmann, G., Chandan, D., Richard Peltier, W., Tan, N., Contoux, C., Ramstein, G., Li, X., Zhang, Z., Guo, C., … Lunt, D. J. (2020). The Pliocene Model Intercomparison Project Phase 2: Large-scale climate features and climate sensitivity. *Climate of the Past*, *16*(6), 2095–2123. https://doi.org/10.5194/cp-16-2095-2020

Herbert, T. D., Lawrence, K. T., Tzanova, A., Peterson, L. C., Caballero-Gill, R., & Kelly, C. S. (2016). Late Miocene global cooling and the rise of modern ecosystems. *Nature Geoscience*, *9*(11), 843–847. https://doi.org/10.1038/ngeo2813

670 Huntington, K. W., Eiler, J. M., Affek, H. P., Guo, W., Bonifacie, M., Yeung, L. Y., Thiagarajan, N., Passey, B., Tripati, A., Daëron, M., & Came, R. (2009). Methods and limitations of "clumped" CO2 isotope (Δ47) analysis by gas-source isotope ratiomass spectrometry. *Journal of Mass Spectrometry*, *44*(9), 1318–1329. https://doi.org/10.1002/jms.1614

Iijima, Y., Fedorov, A. N., Park, H., Suzuki, K., Yabuki, H., Maximov, T. C., & Ohata, T. (2010). Abrupt increases in soil temperatures following increased precipitation in a permafrost region, central Lena River basin, Russia. *Permafrost and*
675 *Periglacial Processes*, *21*(1), 30–41. https://doi.org/10.1002/ppp.662

Intergovernmental Panel on Climate Change (2022). The Ocean and Cryosphere in a Changing Climate: Special Report of the Intergovernmental Panel on Climate Change. *Cambridge University Press.* https://doi.org/https://doi.org/10.1017/9781009157964.

Izokh, N., & Yazikov, A. (2017). Discovery of Early Carboniferous conodonts in Northern Kharaulakh Ranges (lower reaches
680 of the Lena River, northeastern Siberia, Arctic Russia). *Revue de Micropaleontologie*, *60*(2), 213–232. https://doi.org/10.1016/j.revmic.2017.03.001

John, C. M., & Bowen, D. (2016). Community software for challenging isotope analysis: First applications of 'Easotope' to clumped isotopes. *Rapid Communications in Mass Spectrometry*, *30*(21), 2285–2300. https://doi.org/10.1002/rcm.7720

Johnson, K. R., Hu, C., Belshaw, N. S., & Henderson, G. M. (2006). Seasonal trace-element and stable-isotope variations in a
685 Chinese speleothem: The potential for high-resolution paleomonsoon reconstruction. *Earth and Planetary Science Letters*, *244*(1–2), 394–407. https://doi.org/10.1016/j.epsl.2006.01.064

Kokelj, S. V., Tunnicliffe, J., Lacelle, D., Lantz, T. C., Chin, K. S., & Fraser, R. (2015). Increased precipitation drives mega slump development and destabilization of ice-rich permafrost terrain, northwestern Canada. *Global and Planetary Change*, *129*, 56–68. https://doi.org/10.1016/j.gloplacha.2015.02.008

690 Lachniet, M. S. (2009). Climatic and environmental controls on speleothem oxygen-isotope values. *Quaternary Science Reviews*, *28*(5–6), 412–432. https://doi.org/10.1016/j.quascirev.2008.10.021

Lechleitner, F. A., Mason, A. J., Breitenbach, S. F. M., Vaks, A., Haghipour, N., & Henderson, G. M. (2020). Permafrost-related hiatuses in stalagmites: Evaluating the potential for reconstruction of carbon cycle dynamics. *Quaternary Geochronology*, *56*. https://doi.org/10.1016/j.quageo.2019.101037

695 Lewkowicz, A. G., & Way, R. G. (2019). Extremes of summer climate trigger thousands of thermokarst landslides in a High Arctic environment. *Nature Communications*, *10*(1). https://doi.org/10.1038/s41467-019-09314-7

Liang, Y. C., Polvani, L. M., & Mitevski, I. (2022). Arctic amplification, and its seasonal migration, over a wide range of abrupt CO2 forcing. *Npj Climate and Atmospheric Science*, *5*(1). https://doi.org/10.1038/s41612-022-00228-8

Ma, N., Jiang, J. H., Hou, K., Lin, Y., Vu, T., Rosen, P. E., Gu, Y., & Fahy, K. A. (2022). 21st Century Global and Regional
700 Surface Temperature Projections. *Earth and Space Science*, *9*(12). https://doi.org/10.1029/2022EA002662

Mason, A. J., Vaks, A., Breitenbach, S. F. M., Hooker, J. N., & Henderson, G. M. (2022). A simplified isotope dilution approach for the U-Pb dating of speleogenic and other low-232Th carbonates by multi-collector ICP-MS. *Geochronology*, *4*(1), 33–54. https://doi.org/10.5194/gchron-4-33-2022

Masson-Delmotte, Valerie, Zhai, P., Pirani, A., Connors, S. L., Pean, C., Berger, S., Caud, N., Chen, Y., Goldfarb, L., Gomis, M., & others. (2021). Climate change 2021: the physical science basis. *Contribution of Working Group I to the Sixth Assessment Report of the Intergovernmental Panel on Climate Change*, *Cambridge University Press*.

McKay, D. I. A., Staal, A., Abrams, J. F., Winkelmann, R., Sakschewski, B., Loriani, S., Fetzer, I., Cornell, S. E., Rockström, J., & Lenton, T. M. (2022). Exceeding 1.5°C global warming could trigger multiple climate tipping points. *Science*, *377*(6611). https://doi.org/10.1126/science.abn7950

Meinicke, N., Ho, S. L., Hannisdal, B., Nürnberg, D., Tripati, A., Schiebel, R., & Meckler, A. N. (2020). A robust calibration of the clumped isotopes to temperature relationship for foraminifers. *Geochimica et Cosmochimica Acta*, *270*, 160–183. https://doi.org/10.1016/j.gca.2019.11.022

Mikhaltsov et al. (2018). *Russian-German Cooperation: Expeditions to Siberia in 2017* (Jens Strauss, Ed.; pp. 90–107). Alfred-Wegener Institute.

Miller, K. G., Kominz, M. A., Browning, J. V, Wright, J. D., Mountain, G. S., Katz, M. E., Sugarman, P. J., Cramer, B. S., Christie-Blick, N., & Pekar, S. F. (2005). The Phanerozoic Record of Global Sea-Level Change. *Science*, *310*, 1293–1298. https://www.science.org

Miller, G. H., Alley, R. B., Brigham-Grette, J., Fitzpatrick, J. J., Polyak, L., Serreze, M. C., & White, J. W. C. (2010). Arctic amplification: Can the past constrain the future? *Quaternary Science Reviews*, *29*(15–16), 1779–1790. https://doi.org/10.1016/j.quascirev.2010.02.008

Moseley, G. E., Edwards, R. L., Lord, N. S., Spötl, C., & Cheng, H. (2021). Speleothem record of mild and wet mid-Pleistocene climate in northeast Greenland. In *Sci. Adv* (Vol. 7). https://www.science.org

Nazarenko, L. S., Tausnev, N., Russell, G. L., Rind, D., Miller, R. L., Schmidt, G. A., Bauer, S. E., Kelley, M., Ruedy, R., Ackerman, A. S., Aleinov, I., Bauer, M., Bleck, R., Canuto, V., Cesana, G., Cheng, Y., Clune, T. L., Cook, B. I., Cruz, C. A., … Yao, M. S. (2022). Future Climate Change Under SSP Emission Scenarios With GISS-E2.1. *Journal of Advances in Modeling Earth Systems*, *14*(7). https://doi.org/10.1029/2021MS002871

O'Neill, H. B., & Burn, C. R. (2017). Impacts of variations in snow cover on permafrost stability, including simulated snow management, Dempster Highway, Peel Plateau, Northwest Territories. *Arctic Science*, *3*(2), 150–178. https://doi.org/10.1139/as-2016-0036

Opel, T., Bertran, P., Grosse, G., Jones, M., Luetscher, M., Schirrmeister, L., Stadelmaier, K. H., & Veremeeva, A. (2024). Ancient permafrost and past permafrost in the Northern Hemisphere, *Reference Module in Earth Systems and Environmental Sciences*. Elsevier. https://doi.org/https://doi.org/10.1016/B978-0-323-99931-1.00258-0

Orland, I. J., Burstyn, Y., Bar-Matthews, M., Kozdon, R., Ayalon, A., Matthews, A., & Valley, J. W. (2014). Seasonal climate signals (1990-2008) in a modern Soreq Cave stalagmite as revealed by high-resolution geochemical analysis. *Chemical Geology*, *363*, 322–333. https://doi.org/10.1016/j.chemgeo.2013.11.011

Oster, J. L., Ronay, E. R., Sharp, W. D., Breitenbach, S. F. M., & Furbish, D. J. (2023). Controls on Speleothem Initial 234U/238U Ratios in a Monsoon Climate. *Geochemistry, Geophysics, Geosystems*, *24*(4). https://doi.org/10.1029/2023GC010899

Palmtag, J., Obu, J., Kuhry, P., Richter, A., Siewert, M. B., Weiss, N., Westermann, S., & Hugelius, G. (2022). A high spatial resolution soil carbon and nitrogen dataset for the northern permafrost region based on circumpolar land cover upscaling. *Earth System Science Data*, *14*(9), 4095–4110. https://doi.org/10.5194/essd-14-4095-2022

Peel, M. C., Finlayson, B. L., & Mcmahon, T. A. (2007). Hydrology and Earth System Sciences Updated world map of the Köppen-Geiger climate classification. In *Hydrol. Earth Syst. Sci* (Vol. 11). www.hydrol-earth-syst-sci.net/11/1633/2007/

Petersen, S. V., Winkelstern, I. Z., Lohmann, K. C., & Meyer, K. W. (2015). The effects of Porapak(TM) trap temperature on d18O, d13C, and D47 values in preparing samples for clumped isotope analysis. *Rapid Communications in Mass Spectrometry*, *30*(October 2015), 1–10. https://doi.org/10.1002/rcm.7438

Popova, S., Utescher, T., Gromyko, D., Bruch, A. A., & Mosbrugger, V. (2012). Palaeoclimate evolution in siberia and the Russian far east from the oligocene to pliocene - evidence from fruit and seed floras. *Turkish Journal of Earth Sciences*, *21*(2), 315–334. https://doi.org/10.3906/yer-1005-6

Pound, M. J., Haywood, A. M., Salzmann, U., Riding, J. B., Lunt, D. J., & Hunter, S. J. (2011). A Tortonian (Late Miocene, 11.61-7.25Ma) global vegetation reconstruction. *Palaeogeography, Palaeoclimatology, Palaeoecology*, *300*(1–4), 29–45. https://doi.org/10.1016/j.palaeo.2010.11.029

Rae, J. W. B., Zhang, Y. G., Liu, X., Foster, G. L., Stoll, H. M., & Whiteford, R. D. M. (2021). Atmospheric CO 2 over the Past 66 Million Years from Marine Archives. *The Annual Review of Earth and Planetary Sciences*, *49*, 609–650. https://doi.org/10.1146/annurev-earth-082420

Rantanen, M., Karpechko, A. Y., Lipponen, A., Nordling, K., Hyvärinen, O., Ruosteenoja, K., Vihma, T., & Laaksonen, A. (2022). The Arctic has warmed nearly four times faster than the globe since 1979. *Communications Earth and Environment*, *3*(1). https://doi.org/10.1038/s43247-022-00498-3

Schubert, B. A., Jahren, A. H., Davydov, S. P., & Warny, S. (2017). The transitional climate of the late Miocene Arctic: Winter dominated precipitation with high seasonal variability. *Geology*, *45*(5), 447–450. https://doi.org/10.1130/G38746.1

Schuur, E. A. G., McGuire, A. D., Schädel, C., Grosse, G., Harden, J. W., Hayes, D. J., Hugelius, G., Koven, C. D., Kuhry, P., Lawrence, D. M., Natali, S. M., Olefeldt, D., Romanovsky, V. E., Schaefer, K., Turetsky, M. R., Treat, C. C., & Vonk, J. E. (2015). Climate change and the permafrost carbon feedback. In *Nature* (Vol. 520, Issue 7546, pp. 171–179). Nature Publishing Group. https://doi.org/10.1038/nature14338

Sherwin, C. M., & Baldini, J. U. L. (2011). Cave air and hydrological controls on prior calcite precipitation and stalagmite growth rates: Implications for palaeoclimate reconstructions using speleothems. *Geochimica et Cosmochimica Acta*, *75*(14), 3915–3929. https://doi.org/10.1016/j.gca.2011.04.020

Sigmond, M., Fyfe, J. C., & Swart, N. C. (2018). Ice-free Arctic projections under the Paris Agreement. *Nature Climate Change*, *8*(5), 404–408. https://doi.org/10.1038/s41558-018-0124-y

Sliwinski, J. T., Kost, O., Endres, L., Iglesias, M., Haghipour, N., González-Lemos, S., & Stoll, H. M. (2023). Exploring soluble and colloidally transported trace elements in stalagmites: The strontium-yttrium connection. *Geochimica et Cosmochimica Acta*, *343*, 64–83. https://doi.org/10.1016/j.gca.2022.12.023

Smith, D. M., Scaife, A. A., Eade, R., Athanasiadis, P., Bellucci, A., Bethke, I., Bilbao, R., Borchert, L. F., Caron, L. P., Counillon, F., Danabasoglu, G., Delworth, T., Doblas-Reyes, F. J., Dunstone, N. J., Estella-Perez, V., Flavoni, S., Hermanson, L., Keenlyside, N., Kharin, V., … Zhang, L. (2020). North Atlantic climate far more predictable than models imply. *Nature*, *583*(7818), 796–800. https://doi.org/10.1038/s41586-020-2525-0

Spors, S. (2018). Stable Water Isotope Characteristics of Recent Precipitation from Tiksi and Samoylov Island-Calibration of a Geoscientific Proxy for Northern Siberia*: Bachelors Thesis. Institut für Erd- und Umweltwissenschaften, Universität Potsdam.*

Spötl, C., & Vennemann, T. W. (2003). Continuous-flow isotope ratio mass spectrometric analysis of carbonate minerals. In *Rapid Communications in Mass Spectrometry* (Vol. 17, Issue 9, pp. 1004–1006). John Wiley and Sons Ltd. https://doi.org/10.1002/rcm.1010

Stein, R., Fahl, K., Schreck, M., Knorr, G., Niessen, F., Forwick, M., Gebhardt, C., Jensen, L., Kaminski, M., Kopf, A., Matthiessen, J., Jokat, W., & Lohmann, G. (2016). Evidence for ice-free summers in the late Miocene central Arctic Ocean. *Nature Communications*, *7*. https://doi.org/10.1038/ncomms11148

Steinthorsdottir, M., Coxall, H. K., de Boer, A. M., Huber, M., Barbolini, N., Bradshaw, C. D., Burls, N. J., Feakins, S. J., Gasson, E., Henderiks, J., Holbourn, A. E., Kiel, S., Kohn, M. J., Knorr, G., Kürschner, W. M., Lear, C. H., Liebrand, D., Lunt, D. J., Mörs, T., Strömberg, C. A. E. (2021). The Miocene: The Future of the Past. *Paleoceanography and Paleoclimatology*, *36*(4). https://doi.org/10.1029/2020PA004037

Stoll, H. M., Müller, W., & Prieto, M. (2012). I-STAL, a model for interpretation of Mg/Ca, Sr/Ca and Ba/Ca variations in speleothems and its forward and inverse application on seasonal to millennial scales. *Geochemistry, Geophysics, Geosystems*, *13*(1). https://doi.org/10.1029/2012GC004183

Strauss, Fuchs, Hugelius, Miesner, Nitze, Opfergelt, Schuur, Treat, Turetsky, Yang, & Grosse. (2024). Organic matter storage and vulnerability in the permafrost domain. In *Reference Module in Earth Systems and Environmental Sciences*. Elsevier,. https://doi.org/https://doi.org/10.1016/B978-0-323-99931-1.00164-1

Taylor, P. C., Boeke, R. C., Boisvert, L. N., Feldl, N., Henry, M., Huang, Y., Langen, P. L., Liu, W., Pithan, F., Sejas, S. A., & Tan, I. (2022). Process Drivers, Inter-Model Spread, and the Path Forward: A Review of Amplified Arctic Warming. In *Frontiers in Earth Science* (Vol. 9). Frontiers Media S.A. https://doi.org/10.3389/feart.2021.758361

Tooth, A. F., & Fairchild, I. J. (2003). Soil and karst aquifer hydrological controls on the geochemical evolution of speleothem-forming drip waters, Crag Cave, southwest Ireland. *Journal of Hydrology*, *273*.

Treble, P. C., Fairchild, I. J., Griffiths, A., Baker, A., Meredith, K. T., Wood, A., & McGuire, E. (2015). Impacts of cave air ventilation and in-cave prior calcite precipitation on Golgotha Cave dripwater chemistry, southwest Australia. *Quaternary Science Reviews*, *127*, 61–72. https://doi.org/10.1016/j.quascirev.2015.06.001

805 Tremaine, D. M., & Froelich, P. N. (2013). Speleothem trace element signatures: A hydrologic geochemical study of modern cave dripwaters and farmed calcite. *Geochimica et Cosmochimica Acta*, *121*, 522–545. https://doi.org/10.1016/j.gca.2013.07.026

Tremaine, D. M., Froelich, P. N., & Wang, Y. (2011). Speleothem calcite farmed in situ: Modern calibration of δ18O and δ13C paleoclimate proxies in a continuously-monitored natural cave system. *Geochimica et Cosmochimica Acta*, *75*(17), 4929–4950. https://doi.org/10.1016/j.gca.2011.06.005

810

Turetsky, M. R., Abbott, B. W., Jones, M. C., Anthony, K. W., Olefeldt, D., Schuur, E. A. G., Grosse, G., Kuhry, P., Hugelius, G., Koven, C., Lawrence, D. M., Gibson, C., Sannel, A. B. K., & McGuire, A. D. (2020). Carbon release through abrupt permafrost thaw. *Nature Geoscience*, *13*(2), 138–143. https://doi.org/10.1038/s41561-019-0526-0

Vaks, A., Gutareva, O. S., Breitenbach, S. F. M., Avirmed, E., Mason, A. J., Thomas, A. L., Osinzev, A. V., Kononov, A. M.,
815 & Henderson, G. M. (2013). Speleothems reveal 500,000-year history of Siberian permafrost. *Science*, *340*(6129), 183–186. https://doi.org/10.1126/science.1228729

Vaks, A., Mason, A. J., Breitenbach, S. F. M., Kononov, A. M., Osinzev, A. V., Rosensaft, M., Borshevsky, A., Gutareva, O. S., & Henderson, G. M. (2020). Palaeoclimate evidence of vulnerable permafrost during times of low sea ice. *Nature*, *577*(7789), 221–225. https://doi.org/10.1038/s41586-019-1880-1

820 Vaks, A., Mason, A., Breitenbach, S.F.M., Giesche, A., Osintzev, A., Yakshina., I., Kononov, A., Umbo, S., Rosensaft, M. Borshevsky, A., and Henderson, G. M. (2024). Arctic speleothems reveal largely permafrost-free Northern Hemisphere during the Late Miocene, [Manuscript in review]

Wang, P., Huang, Q., Tang, Q., Chen, X., Yu, J., Pozdniakov, S. P., & Wang, T. (2021). Increasing annual and extreme precipitation in permafrost-dominated Siberia during 1959–2018. *Journal of Hydrology*, *603*.
825 https://doi.org/10.1016/j.jhydrol.2021.126865

Wassenburg, J. A., Riechelmann, S., Schröder-Ritzrau, A., Riechelmann, D. F. C., Richter, D. K., Immenhauser, A., Terente, M., Constantin, S., Hachenberg, A., Hansen, M., & Scholz, D. (2020). Calcite Mg and Sr partition coefficients in cave environments: Implications for interpreting prior calcite precipitation in speleothems. *Geochimica et Cosmochimica Acta*, *269*, 581–596. https://doi.org/10.1016/j.gca.2019.11.011

830 Wassenburg, J. A., Immenhauser, A., Richter, D. K., Jochum, K. P., Fietzke, J., Deininger, M., Goos, M., Scholz, D., & Sabaoui, A. (2012). Climate and cave control on Pleistocene/Holocene calcite-to-aragonite transitions in speleothems from Morocco: Elemental and isotopic evidence. *Geochimica et Cosmochimica Acta*, *92*, 23–47. https://doi.org/10.1016/j.gca.2012.06.002

Xie, A., Zhu, J., Kang, S., Qin, X., Xu, B., & Wang, Y. (2022). Polar amplification comparison among Earth's three poles

835   under different socioeconomic scenarios from CMIP6 surface air temperature. *Scientific Reports*, *12*(1).
https://doi.org/10.1038/s41598-022-21060-3

York, D., Evensen, N. M., Martínez, M. L., & De Basabe Delgado, J. (2004). Unified equations for the slope, intercept, and
standard errors of the best straight line. *American Journal of Physics*, *72*(3), 367–375. https://doi.org/10.1119/1.1632486

840